QUASI-INCOMPRESSIBLE AND QUASI-INEXTENSIBLE ELEMENT AND
MATERIAL FORMULATION FOR ANISOTROPIC MEDIUM

A THESIS SUBMITTED TO
THE GRADUATE SCHOOL OF NATURAL AND APPLIED SCIENCES
OF
MIDDLE EAST TECHNICAL UNIVERSITY

BY

BURAK RODOPLU

IN PARTIAL FULFILLMENT OF THE REQUIREMENTS
FOR
THE DEGREE OF MASTER OF SCIENCE
IN
MECHANICAL ENGINEERING

MARCH 2018

Approval of the thesis:

QUASI-INCOMPRESSIBLE AND QUASI-INEXTENSIBLE ELEMENT AND MATERIAL FORMULATION FOR ANISOTROPIC MEDIUM

submitted by **BURAK RODOPLU** in partial fulfillment of the requirements for the degree of **Master of Science in Mechanical Engineering Department, Middle East Technical University** by,

Prof. Dr. Halil Kalıpçılar
Dean, Graduate School of **Natural and Applied Sciences** ⎯⎯⎯⎯⎯⎯

Prof. Dr. M.A. Sahir Arıkan
Head of Department, **Mechanical Engineering** ⎯⎯⎯⎯⎯⎯

Assist. Prof. Dr. Hüsnü Dal
Supervisor, **Mechanical Engineering Department, METU** ⎯⎯⎯⎯⎯⎯

Examining Committee Members:

Prof. Dr. Suha Oral
Mechanical Engineering Department, METU ⎯⎯⎯⎯⎯⎯

Assist. Prof. Dr. Hüsnü Dal
Mechanical Engineering Department, METU ⎯⎯⎯⎯⎯⎯

Prof. Dr. Suat Kadıoğlu
Mechanical Engineering Department, METU ⎯⎯⎯⎯⎯⎯

Assoc. Prof. Dr. Ercan Gürses
Aerospace Engineering Department, METU ⎯⎯⎯⎯⎯⎯

Assoc. Prof. Dr. Cihan Tekoğlu
Mechanical Engineering Department, TOBB University of
Economics and Technology ⎯⎯⎯⎯⎯⎯

Date: **30.03.2018**

I hereby declare that all information in this document has been obtained and presented in accordance with academic rules and ethical conduct. I also declare that, as required by these rules and conduct, I have fully cited and referenced all material and results that are not original to this work.

Name, Last Name: BURAK RODOPLU

Signature   :

ABSTRACT

QUASI-INCOMPRESSIBLE AND QUASI-INEXTENSIBLE ELEMENT AND MATERIAL FORMULATION FOR ANISOTROPIC MEDIUM

RODOPLU, Burak

M.S., Department of Mechanical Engineering

Supervisor   : Assist. Prof. Dr. Hüsnü Dal

March 2018, 62 pages

The contribution presents a *novel* finite element formulation for quasi-inextensible and quasi-incompressible finite hyperelastic behavior of transversely anisotropic materials and addresses its computational aspects. The formulation is presented in purely *Eulerian* setting and based on the additive decomposition of the free energy function into isotropic and anisotropic parts where the isotropic part is further decomposed into isochoric and volumetric parts. For the quasi-incompressible response, the *Q1P0* element formulation is outlined briefly where the pressure type Lagrange multiplier and its conjugate enter the variational formulation as an extended set of variables. Using the similar argumentation, an extended Hu-Washizu type potential is introduced where the average volume fiber stretch and fiber stress are additional field variables. Within this context, the resulting Euler-Lagrange equations and the element formulation resulting from the extended variational principle are derived. The numerical implementation exploits the underlying variational structure leading to a canonical symmetric structure. The efficiency of the proposed approached is demonstrated through representative boundary value problems. The superiority of the proposed element formulation over the standard *Q1*- and *Q1P0-element formulation* is studied through convergence analyses. The proposed finite element formulation is modular and shows excellent performance for fiber reinforced materials in the inextensibility limit. Moreover, performance of the proposed formulation is studied for representa-

tive boundary value problems applied to soft biological tissues such as human arterial wall.

ÖZ

ANİZOTROPİK MALZEMELER İÇİN YARI-SIKIŞTIRILAMAZ VE YARI-UZATILAMAZ ELEMAN VE MALZEME FORMÜLASYONU

RODOPLU, Burak

Yüksek Lisans, Makina Mühendisliği Bölümü

Tez Yöneticisi   : Dr. Öğr. Üyesi Hüsnü Dal

Mart 2018 , 62 sayfa

Bu tez anizotropik malzemelerin yarı-sıkıştırılamaz ve yarı-uzatılamaz hiper elastik davranışları için yeni sonlu elemanlar formülasyonu sunmaktadır ve hesaba dayalı konularına girmektedir. Sunulan formülasyon Euler formunda, malzemenin deforme olmuş halinde, verilmektedir ve serbest enerji fonksiyonunun anizotropik ve izotropik olarak ayrıştırılmasına dayanmaktadır. Bunun yanında serbest enerji fonksiyonunun izotropik kısmı hacimsel ve izokorik olarak ayrıştırılmıştır. *Q1P0* eleman formülasyonu yarı-sıkıştırılamaz davranışı modellemek için anlatılacaktır. Bu formülasyonda basınç tipi Lagrange çarpanı ve onun çifti varyasyonel formülasyona genişletilmiş değişken olarak girmektedir. Benzer yaklaşım kullanılarak, genişletilmiş Hu-Washizu tipi potansiyel sunulmaktadır. Bu yaklaşımda, ekstradan ortalama fiber uzaması ve fiber gerilimi alan değişkeni olarak eklenmiştir. Bu anlamda ortaya çıkan Euler-Lagrange denklemleri ile birlikte genişletilmiş varyasyonel prensipten oluşan eleman formülasyonu türetilmiştir. Bu yaklaşımın verimliliği örnek sınır değerli problemler üzerinde test edilmiştir. Bunun yanında, önerilen formülasyonla standart eleman formülasyonu, *Q1*, ve *Q1P0* eleman formülasyonu yakınsama çalışmaları yapılarak karşılaştırılmıştır. Önerilen *Q1P0F0* eleman formülasyonu anizotropik malzemeler için diğer formülasyonlara nazaran daha iyi performans göstermiştir. Bunun yanında önerilen formülasyonun performansı biyolojik dokular üzerinde çeşitli örnekler kullanılarak test edilmiştir.

Anahtar Kelimeler: anizotropi, hiper elastikiyet, yarı-sıkıştırılamaz, yarı-uzatılamaz, karışık sonlu elemanlar, karışık varyasyonel prensipler

to my wife Çağla

and

to my son Toprak

ACKNOWLEDGMENTS

TABLE OF CONTENTS

LIST OF TABLES

TABLES

LIST OF FIGURES

FIGURES

xiv

CHAPTER 1

INTRODUCTION

Biological tissues and wood are some examples of natural anisotropic materials. Arterial wall is one of the example of anisotropic biological tissues. Arterial wall consists of mainly three layers as it can be seen in Figure 1.1 [20]. These three layers are the innermost layer, intima, middle layer, media, and outermost layer, adventitia. They contain fibers inside them and direction of the fibers are different for each layer. Behavior of each layer is studied by Holzapfel [22]. Arterial wall for soft biological tissues shows exponential stiffening effect at high pressure values, because, as the pressure increases there becomes gradual straightening and further elongation of collagen fibers [20]. This behavior can be seen from Figure 1.2 (a-b) clearly. Figure 1.2 (a) shows the material behavior curve of the arterial wall under uniaxial loading in fiber direction. As the axial stretch increases, axial stress increases sharply with exponential behavior.

On the other hand, there are some man-made anisotropic materials, e.g. fiber reinforced materials and composites. These manufactured anisotropic materials are used in various areas such as automotive and aerospace industries. For example, Figure 1.3 shows a Boeing 787 aircraft. Almost 60% of the aircraft is made from anisotropic materials. The aircraft mostly contains carbon laminates.

1.1 Finite Element Formulation

Shear locking is the one of the problems that are encountered in finite element analysis. Using linear elements is the main reason of this problem. Under bending loading, linear elements introduce fictitious shear stress because of incorrect modelling of the
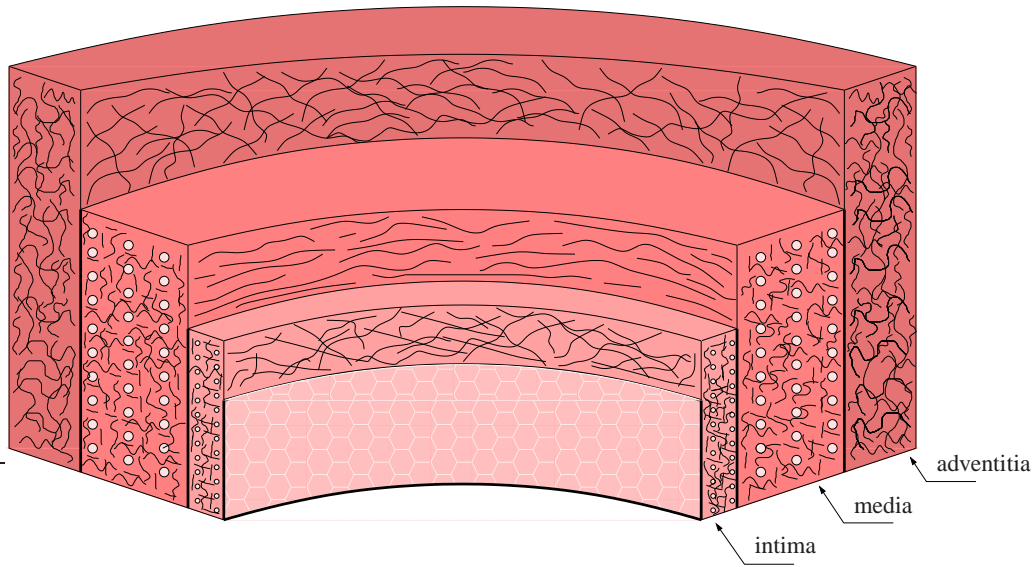
Figure 1.1: Layers of the arterial wall as intima, media and adventitia [20].
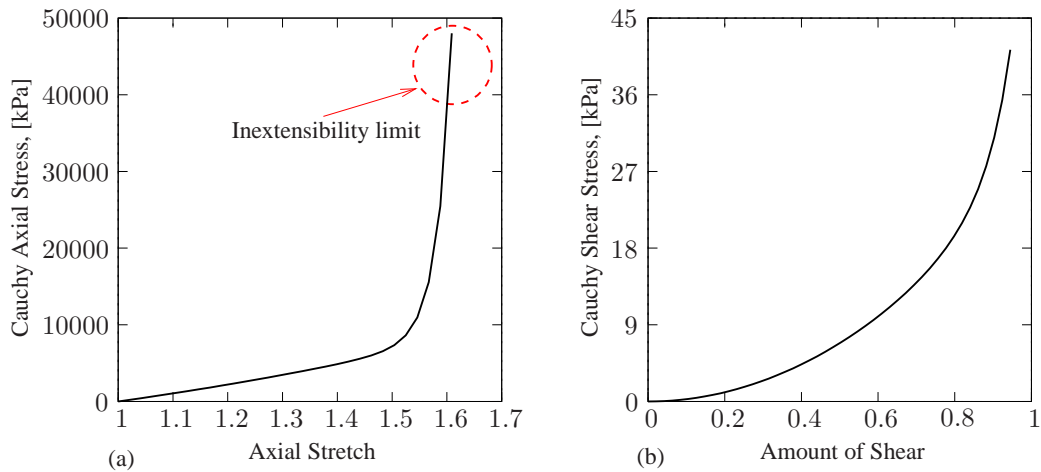
Figure 1.2: Material behavior curves of arterial wall for (a) axial stress-axial stretch under uniaxial loading and (b) out of plane shear stress-amount of shear under simple shear loading.

curvature in an element. Therefore, the element comes to equilibrium with smaller bending displacements because of the shear stress. Then, it can be said that the locking problem causes the element to behave stiffer than actual behavior.

Different type of the locking, named as volumetric locking, occurs for some of the anisotropic materials, such as biological tissues. These materials show very stiff volumetric response compared to bulk shear response which means nearly incompressible behavior. This incompressible behavior causes the *locking phenomena*. The standard displacement based finite element formulations show very poor performance in the

2

Figure 1.3: Boeing 787 Aircraft [10].

quasi-incompressible limit where bulk modulus is much higher than shear modulus. The main reason of this situation is that the volume remains constant at each integration point of the element and this overconstraints the displacement field. Therefore, the standard shape functions can include the incompressibility constraint by causing artificial stiffening [27, 28].

Moreover, some of these anisotropic materials, such as fiber-reinforced composites and biological tissues, exhibit much higher stiffness in the direction of the fiber compared to transverse direction. This behavior can be seen from Figure 1.2 (a-b). Figure 1.2 (a) shows the behavior of arterial wall in fiber direction under uniaxial loading while Figure 1.2 (b) shows the behavior of arterial wall in transverse direction under simple shear. It is clearly seen that material exhibits much higher stiffness in the direction of fiber when stress results are compared. This causes the same mathematical problem in the inextensibility limit. Also, inextensibility limit region can be seen from Figure 1.2 (a). Therefore building robust and efficient finite element formulation for such anisotropic materials in the quasi-incompressible and quasi-inextensible limits is an interesting topic.

Using *h*- or *p*-refinement strategies can be one of the solutions to the problem. Simply, *h*-refinement means that number of the lower order elements is increased for better solution, while higher order polynomials are used by keeping number of elements constant in *p*-refinement technique. It is a fact that locking response is known to disappear for higher order triangles $p > 4$ [52] and computational cost is increased by using lower order elements with *h*-refinement. Nevertheless, since lower order elements are more simple and robust than the higher order elements in case of nonlinear Lagrangian hyperelastic formulations, they still preserve their popularity [53]. Therefore, performance of the standard lower order elements has been tried to be improved for the last decades.

Moreover, locking problem can be solved by different methods such as *reduced integration*, *stabilization*, *mixed or hybrid element formulations* [61]. *Mixed* or *hybrid element formulations* are types of variational methods where an additional stress or strain type penalty term is defined as a Lagrange multiplier. The first hybrid formulation of linear elasticity was offered by Pian et al. [43, 42, 44]. The formulation consists of Hellinger–Reissner variational principle for linear elastic medium. Also, this formulation enhances stress approximation of the standard displacement formulations under extreme deformation. Matrix inversion of the elasticity tensor at element level is required and is not easy in case of nonlinear elasticity at finite strains [2]. *Reduced integration schemes* along with *stabilization techniques* is another strategy to enhance the behavior of the linear pure displacement formulation against locking problem [27, 32]. The assembly of the tangent and residual terms of polynomial shape functions using less number of Gauss points than required can be followed with the research of Zienkiewicz et al. [66]. However, reduced integration method can cause *hourglass modes* or *zero energy modes*. *Hourglass modes* or *zero energy modes* can be explained such that element distortion does not generate strain energy because of reduced number of integration points. This problem leads to meaningless results, especially for coarse meshes. Therefore, *Hourglass modes* caused by the reduced integration should be stabilized [7, 48]. Hourglass stabilization methods are computationally applicable because they decrease the number of computations at element level. However, stabilization requires additional nonphysical parameters into formulation which can affect the results under bending dominated cases. Also, *enhanced strain*

formulations (ESF) based on the introduction of auxiliary incompatible strain field satisfying the material frame invariance and objectivity requirements were developed [6, 54, 53, 55, 56] for finite strain elasticity and elastoplasticity problems. These formulations are based on Hu–Washizu type variational principles. Moreover, extension of them to the higher order gradient plasticity has been studied in [37, 38, 39]. Enhanced strain formulations do not require the modification of the constitutive model but nonlinear formulation create non-physical instabilities on element. These instabilities cannot be eliminated by increasing the order of quadrature and modifying the material model. Canceling terms at the element level can be introduced in order to minimize these hour-glass type instabilities [19, 29]. With the help of these formulations, hourglass modes can be eliminated under compression but numerical stability cannot be guaranteed for irregular distorted meshes and nonhomogeneous stress states. This hourglass instabilities can be solved for highly distorted meshes with the separation of element tangent matrix into constant and hourglass parts, and by introducing a control technique based on a modal analysis [49, 62].

Q1P0 element formulation was firstly mentioned by Nagtegaal et al. [40]. The formulation is also named as the *mean dilatation approach*. It is worked in Brezzi & Fortin [15] for small strain cases and enlarged to large strain problems by Simó et al. [58]. Simó & Taylor [57] used the formulation for hyperelastic materials in the quasi-incompressibility limit. Enforcing incompressibility is achieved by introducing an additional term into the potential functional which behaves as constraint. *Q1P0* element formulation is studied in detail in literature [36, 61]. The formulation is improved to get better performance in bending dominated problems. Then, the formulation is enlarged to the finite element implementation of elasto-plastic material response [13] and transversely anisotropic materials and soft tissues [60].

Ladyzhenskaya-Babuska-Brezi (LBB) condition known as *inf-sup condition* is used to justify the stability of mixed finite element method [3, 11, 30]. Also, stability for incompressible condition in linear elasticity is worked in [5]. However, *LBB condition* study is not trivial for finite strain condition because *Q1P0* element formulation fails to fulfill the *inf-sup condition* [61]. On the other hand, it is confirmed that formulation is stable for a wide range of applications in quasi-incompressibility condition undergoing large deformations [36].

1.2 Constitutive Model

Three invariants $\{I_1, I_2, I_3\}$ are used to model the free energy function for isotropic materials. Moreover, $\{I_1, I_2\}$ invariants are enough to define the incompressible isotropic behavior. The invariants and constitutive formulations will be defined in Chapter 2 in detail.

In order to describe transversely isotropic behavior, additional two invariants $\{I_4, I_5\}$, generated by Cauchy Green tensor and reference unit vector, are introduced [9, 8, 50]. In fiber reinforced materials, free energy function uses unreinforced base matrix enlarged by the fourth invariant I_4 as an additional penalty function for stretching in the fiber direction [46]. Similar method is applied to soft biological tissues [23]. *Standard reinforcing model* is the name of the proposed function [46]. In this model there are instabilities under simple shear, and uniaxial compression when the fiber stiffness increases. Then, the material instability as loss of ellipticity of the standard reinforcing model is studied in [47, 34, 35]. Moreover, inextensibility is worked for transversely isotropic solid with unidirectional reinforcement in [1].

In literature, free energy function is divided into volumetric, isochoric and anisotropic parts. Volumetric part is a function of $J = \det \boldsymbol{F}$ and an isochoric part is a function of the unimodular part of the deformation gradient which is $\bar{\boldsymbol{F}} = J^{-1/3}\boldsymbol{F}$ [17]. For the isotropic region, split of volumetric and isochoric parts has lots of advantages in the incompressible region. For instance, the split leads to easy implementation of the *mean dilatation approach* into the finite element formulation. However, the split can cause fictitious results in the compressible region [14]. Then it is described that split of volumetric and isochoric parts should be applied only to the matrix part.

Moreover, a similar problem has been detected for the split of anisotropic part of the free energy. It is shown that use of the fourth invariant $\bar{I}_4$ of the unimodular stretch tensor creates similar fictitious results for uniaxial tension test in [21]. In the work, uniaxial stress creates volume increase at small stretches causing negative Poisson ratio ν because exponential anisotropic free energy function competes with volumetric free energy function in the quasi inextensibility limit all through the minimization of the strain energy. This problem can be overcome by using the anisotropic free energy

6

function $\psi_{ani} = \psi_{ani}(I_4)$ in terms of the fourth invariant of the deformation tensor.

In recent times, Hu-Washizu type mixed variational principles have been examined to develop the formulation for inextensibility limit in biological tissues and fiber reinforced elastomers in [51, 63, 64, 65]. Therein, Zdunek et al. [64, 65] propose a model based on the kinematic split of the deformation gradient into a purely spherical part, a purely unimodular extensional part and an extension free unimodular tensor. The Lagrangian element formulation using scalar conjugate pairs (p, θ) and (ρ, λ) for pressure-dilatation and fiber stress-stretch is parallel to the mean dilatational approach [58] (MDA). Then a five fields variational formulation which arises where the consistent linearization and static condensation at element level causes purely displacement element matrix. Convergence and stability of the solution are not shown in the formulation. However, the models of the Schröder et al. [51] and Wriggers et al. [63] are mixed models combining mean dilatational approach for quasi incompressibility and enhanced strain formulation for quasi-inextensibility by using extra deformation measure in variational formula. In the formulation basic kinematic approach is used where strain energy consists of extra decomposed isotropic and anisotropic parts.

Anisotropic part of the free energy function ψ_{ani} for the biological tissues, especially arteries, is worked in [26, 18, 24, 25, 4]. They propose some kinds of anisotropic part of the free energy function. Firstly, one of the suggested anisotropic part of free energy function consists of an exponential function by including a material parameter and a non-dimensional constant, k_1 and k_2, respectively, given in the work of Holzapfel et al. [24]. Various kinds of fiber modelling for arteries are studied in the review of Gasser et al. [18]. One of these models is fiber dispersion model for the anisotropic free energy function. They use a single structure parameter in the ψ_{ani} to represent the effects of collagen fiber distribution in an integral sense. Also, Holzapfel & Ogden [25] use similar modelling of the anisotropic free energy function for the passive myocardium. Most of these references use an exponential function for the anisotropic part of the free energy function for arteries.

Moreover, determination of these material and non-dimensional parameters, k_1 and k_2, is another important topic. This topic is examined in detail by [22, 16, 59]. In these works, constitutive parameters for the aortas are determined for various age and

gender combinations of humans and average values for parameters are given. Studies are also conducted for different regions of aortas such as abdominal and throacic. Balzini & Holzapfel [4] offer constitutive constants for the media region of a human carotid artery in the physiological loading domain, also Li et al. [31] offer material constants for a human carotid artery. Moreover, material parameters for the human iliac arteries are given in the research of Qi et al. [45]. Also, material parameters for the passive myocardium are given in [25]. Furthermore, geometric parameters of the layers of the aortas are examined in the work of the Holzapfel & Ogden [26].

In this work, theoretical and computational settings for almost incompressible and inextensible material behavior depending on a saddle point principle obtained from a mixed potential will be presented. Also, a five-field Hu-Washizu type extended variational formulation will be studied in the work. To summarize, mixed finite element formulation which is an extended version of *Q1P0* formulation to inextensibility limit will be proposed in this study. Free energy function is decomposed into purely volumetric, isochoric and anisotropic parts. A similar exponential function for the anisotropic part will be used in the work. Also, deformation gradient is divided into two parts as unimodular and spherical. Moreover, anisotropic behavior is given by using the fourth invariant with the simplified approach. A scalar kinematic variable, λ, and a Lagrange multiplier, s, are used to enforce quasi inextensibility. An eight-noded brick element is represented in the finite element formulation. However, it can be combined with linear and higher order element formulations in a straightforward manner.

After Chapter 1, theory including equation of motion, constitutive modelling, mixed variational formulation and finite element formulation will be examined in detail in Chapter 2. Then, the proposed model will be compared with the existing models on a simple example in Chapter 3. After validation, the proposed formulation will be applied to a combined loading of the arterial wall which has more realistic geometry and material parameters to see the behavior of the arteries in Chapter 4. Finally, the thesis will be concluded with the conclusion and future work part in Chapter 5.

THEORY

2.1 Governing equations of motion

Field equations and corresponding state variables of a transversely isotropic hyperelastic solid body are presented in this section. This section also contains the introduction of the kinematics and integrity basis of the deformation and the constitutive equations based on a Neo-Hookean hyperelastic model. Finally, the model is extended to transverse anisotropy through standard reinforcing model.

2.1.1 Geometric mappings and the field variables

A *body* $\mathscr{B}$ is a 3-D structure including material points $\mathscr{P} \in \mathscr{B}$ and its motion as a function of time is defined by using bijective mappings as

$$\boldsymbol{\chi}(\mathscr{P},t) = \begin{cases} \mathscr{B} & \to & \mathscr{B}(\mathscr{P},t) \in \mathbb{R}^3 \times \mathbb{R}_+ \\ \mathscr{P} & \mapsto & \boldsymbol{x} = \boldsymbol{\chi}_t(\mathscr{P}) = \boldsymbol{\chi}(\mathscr{P},t). \end{cases} \tag{2.1}$$

The point $\boldsymbol{x} = \boldsymbol{\chi}(\mathscr{P},t)$ stands for the position of the particle $\mathscr{P}$ at time $t \in \mathbb{R}_+$. Also, $\boldsymbol{X} = \boldsymbol{\chi}(\mathscr{P},t_0) \in \mathbb{R}^3$ can be defined as the location of material points at a reference time t_0 and $\boldsymbol{\chi}_t(\mathscr{P}) = \boldsymbol{\chi}(\mathscr{P},t)$ can be defined as the position map for a frozen time frame t. Moreover, $\boldsymbol{\varphi}_t = \boldsymbol{\chi}_t \circ \boldsymbol{\chi}_{t_0}^{-1}(\boldsymbol{X})$ denotes deformation map such as

$$\boldsymbol{\varphi}_t(\boldsymbol{X}) = \begin{cases} \mathscr{B}_0 & \to & \mathscr{B} \in \mathbb{R}^3 \\ \boldsymbol{X} & \mapsto & \boldsymbol{x} = \boldsymbol{\varphi}(\boldsymbol{X},t) \end{cases} \tag{2.2}$$
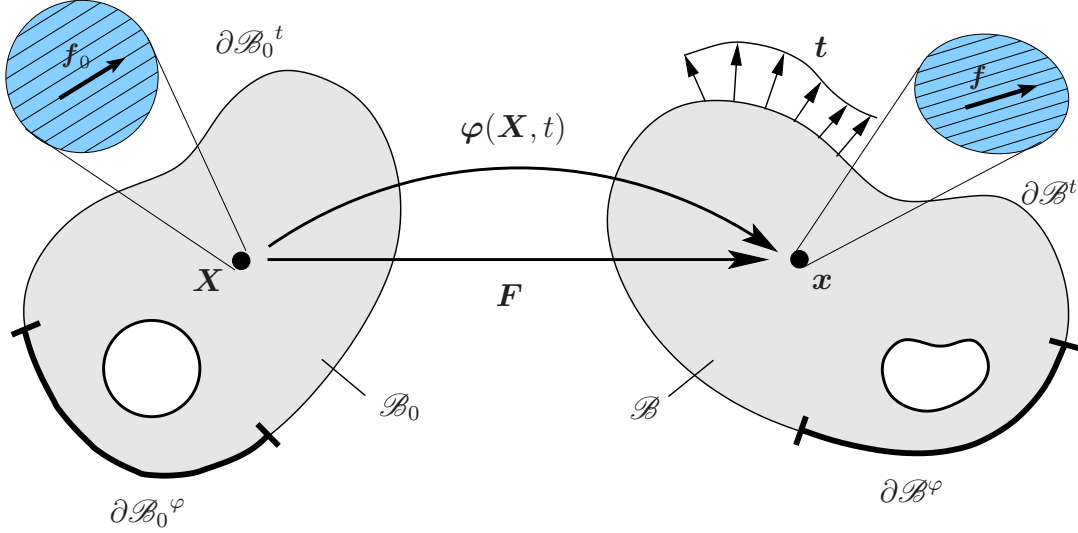
Figure 2.1: Nonlinear deformation of a body [12].

maps the reference configuration $\boldsymbol{X} \in \mathscr{B}_0$ of a material point on the spatial configuration $\boldsymbol{x} \in \mathscr{B}$. The *deformation gradient* can be defined as

$$\boldsymbol{F} : T_X\mathscr{B}_0 \to T_x\mathscr{B}; \quad \boldsymbol{F} := \nabla_X\boldsymbol{\varphi}_t(\boldsymbol{X}). \tag{2.3}$$

The deformation gradient maps the unit tangent of the *Lagrangian* (reference) configuration which is T_X onto its counterpart in the *Eulerian* (current) configuration which is T_x. The operators $\nabla_X[\bullet]$ and $\nabla_x[\bullet]$ can be defined as the spatial derivatives with respect to the reference $\boldsymbol{X}$ and current $\boldsymbol{x}$ coordinates. Also the cofactor of the deformation gradient and the Jacobian can be defined as

$$\mathrm{cof}[\boldsymbol{F}] = \det[\boldsymbol{F}]\boldsymbol{F}^{-T} \quad \text{and} \quad J := \det[\boldsymbol{F}] > 0. \tag{2.4}$$

Note that the condition $J := \det[\boldsymbol{F}] > 0$ guarantees impenetrable deformation $\boldsymbol{\varphi}$. Then, the deformation gradient defines the deformation of an infinitesimal line, area and volume element, respectively, as

$$d\boldsymbol{x} = \boldsymbol{F}d\boldsymbol{X}\ , \quad d\boldsymbol{a} = \mathrm{cof}[\boldsymbol{F}]d\boldsymbol{A}\ , \quad dv = JdV\ , \tag{2.5}$$

where $d\boldsymbol{X}$, $d\boldsymbol{A}$ and dV, respectively, can be defined as the infinitesimal line, area

10
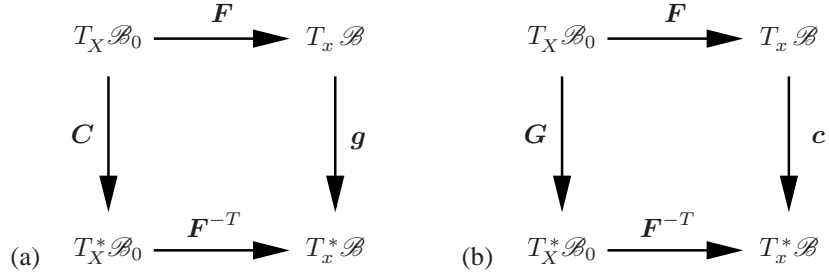
Figure 2.2: Definition of *right and left Cauchy Green tensors*. (a) *Current metric* in Lagrangian configuration. (b) *Reference metric* in Eulerian configuration.

and volume element in the undeformed state. Figure 2.1 shows the general sketch of the nonlinear deformation map. In the Figure 2.1, the reference configuration is $\mathscr{B}_0 \in \mathbb{R}^3$ and the spatial configuration is $\mathscr{B} \in \mathbb{R}^3$. $\varphi : \mathscr{B} \times \mathbb{R} \mapsto \mathbb{R}^3$ is the nonlinear deformation map which maps at time $t \in \mathbb{R}_+$ material point position $X \in \mathscr{B}_0$ onto spatial position $x = \varphi(X, t) \in \mathscr{B}$. The deformation gradient F maps a Lagrangian line element dX onto its Eulerian counterpart dx.

Moreover, the *right Cauchy Green tensor* and the inverse of the *left Cauchy Green tensors* can be defined as

$$C = F^T g F, \tag{2.6}$$

$$c = F^{-T} G F^{-1}, \tag{2.7}$$

where g and G are the current and reference metric tensors in the neighborhoods $\mathbb{N}_X$ of X and $\mathbb{N}_x$ of x, respectively. These tensors are used for the mapping between the co- and contravariant objects in the reference $\mathscr{B}_0$ and the spatial $\mathscr{B}$ manifolds [33]. Also, the *left Cauchy Green tensor* or the *Finger tensor* can be defined as

$$b = c^{-1}. \tag{2.8}$$

Figure 2.2 (a-b) is useful for geometrical interpretation of these tensors. Figure 2.2 (a) interprets the *right Cauchy Green tensor* defined in (2.6), and Figure 2.2 (b) interprets the *left Cauchy Green tensor* defined in (2.7).

Then, the deformation gradient is divided into volumetric and unimodular parts in

11

order to impose the quasi-incompressible behavior of soft biological tissues as

$$\boldsymbol{F}_{vol} := J^{1/3}\boldsymbol{1} \qquad \text{and} \qquad \bar{\boldsymbol{F}} := J^{-1/3}\boldsymbol{F}, \tag{2.9}$$

where

$$\boldsymbol{F} = \boldsymbol{F}_{vol}\bar{\boldsymbol{F}} . \tag{2.10}$$

The Lagrangian unit vector $\boldsymbol{f}_0$ is introduced to reflect anisotropic continuum. Under the presence of $\boldsymbol{\varphi}_t$, the Eulerian counterpart can be defined as

$$\boldsymbol{f} = \boldsymbol{F}\boldsymbol{f}_0 . \tag{2.11}$$

Also, the boundaries of solid domain can be divided into Dirichlet and Neumann-type boundaries such that

$$\partial\mathscr{B} = \partial\mathscr{B}^\varphi \cup \partial\mathscr{B}^t \qquad \text{and} \qquad \partial\mathscr{B}^\varphi \cap \partial\mathscr{B}^t = \emptyset. \tag{2.12}$$

2.1.1.1   Stress tensors

We define a part $\mathscr{P}_0 \subset \mathscr{B}_0$ extracted from the reference configuration $\mathscr{B}_0$ and its spatial counterpart $\mathscr{P}_t \subset \mathscr{B}_t$ with boundaries $\partial\mathscr{P}_0$ and $\partial\mathscr{P}_t$. $\boldsymbol{t}$ can be defined as the total stress vector and acts on the the surface element $d\boldsymbol{a} \subset \partial\mathscr{P}_t$ on the deformed state. The total stress vector can be introduced by using Cauchy's stress theorem as

$$\boldsymbol{t}(\boldsymbol{x}, t; \boldsymbol{n}) = \boldsymbol{\sigma} \cdot \boldsymbol{n}, \tag{2.13}$$

where $\boldsymbol{\sigma}$ is Cauchy stress tensor. Then the Lagrangian and Eulerian unit area elements can be defined as

$$d\boldsymbol{A} = \boldsymbol{N}dA \quad \text{and} \quad d\boldsymbol{a} = \boldsymbol{n}da , \tag{2.14}$$

12

where N and n are the surface normals of the undeformed and deformed configuration. Then by using equality $T d A = t d a$ the nominal stress tensor P can be defined as

$$P dA = \boldsymbol{\sigma} da \qquad \text{where} \qquad P = J \boldsymbol{\sigma} F^{-T}. \tag{2.15}$$

2.1.2 Constitutive model: Transversely isotropic neoHookean model

As it is mentioned in the previous chapters, fiber reinforced materials and biological tissues exhibit nearly incompressible bulk response and inextensible behavior in the fiber direction. Figure 2.3 simply demonstrates a schematic for a fiber reinforced composites. Free energy function can be defined for this kind of materials in the form such as

$$\psi(\boldsymbol{g}; \boldsymbol{F}, \boldsymbol{f}_0) = \psi_{vol}(J) + \psi_{iso}(\boldsymbol{g}; \bar{\boldsymbol{F}}) + \psi_{ani}(\boldsymbol{g}; \boldsymbol{F}, \boldsymbol{f}_0), \tag{2.16}$$

divided into three parts as volumetric, isochoric and anisotropic, respectively. *Q1P0F0* mixed-element formulation for biological tissues is generated by using a quasi-incompressible Neo-Hookean type hyperelastic formulation in the decoupled form (2.16). However, the proposed formulation can be used in combination of any isotropic hyperelastic solid model because of the generality. The free energy function for an isotropic hyperelastic material is constructed by using three invariants as

$$I_1 = \operatorname{tr} \boldsymbol{C}, \tag{2.17}$$

$$I_2 = \frac{1}{2} \left[I_1^2 - \operatorname{tr}(\boldsymbol{C}^2) \right], \tag{2.18}$$

$$I_3 = \det \boldsymbol{C} = J^2, \tag{2.19}$$

where C is the right Cauchy Green tensor defined in (2.6).

13

Furthermore, the anisotropic response of the material is generated by introducing additional invariants. Therefore, the two additional invariants are introduced in terms of the reference unit vector $\boldsymbol{f}_0$

$$I_4 := \boldsymbol{f}_0 \cdot \boldsymbol{C} \boldsymbol{f}_0 \qquad I_5 = \boldsymbol{f}_0 \cdot \boldsymbol{C}^2 \boldsymbol{f}_0, \tag{2.20}$$

which is used to model the energy storage of the a single fiber reinforced microstructure.

Then, the parts of the free energy function defined in (2.16) can be modelled by using these invariants. Firstly, the volumetric part of the free energy function is defined as;

$$\psi_{vol}(J) = \frac{\kappa}{4} \left(J^2 - 2 \ln J - 1 \right), \tag{2.21}$$

which constrains the quasi-incompressible material behavior [41]. The isochoric part of the free energy function is defined by using a Neo-Hookean model.

$$\psi_{iso}(\boldsymbol{g}; \bar{\boldsymbol{F}}) = c_1 (\bar{I}_1 - 3). \tag{2.22}$$

Note that $2c_1 = \mu_0$ is the initial shear modulus. The anisotropic part of the free energy function for the biological tissues can be defined as

$$\psi_{ani}(\boldsymbol{g}; \boldsymbol{F}, \boldsymbol{f}_0) = \frac{k_1}{k_2} (\exp[k_2 \langle I_4 - 1 \rangle^2] - 1), \tag{2.23}$$

which consists of an exponential function of the fourth invariant. The function is suitable for the arteries taken from [18]. Also, the Macauley brackets $\langle \bullet \rangle$ filter out the tensile deformations and it can be defined as

$$\langle \bullet \rangle = \frac{| \bullet | + (\bullet)}{2}. \tag{2.24}$$

If two families of fibers are used, there should be a new invariant, I_6, which represents other family of fibers with a new reference unit vector $\boldsymbol{f}'_0$.
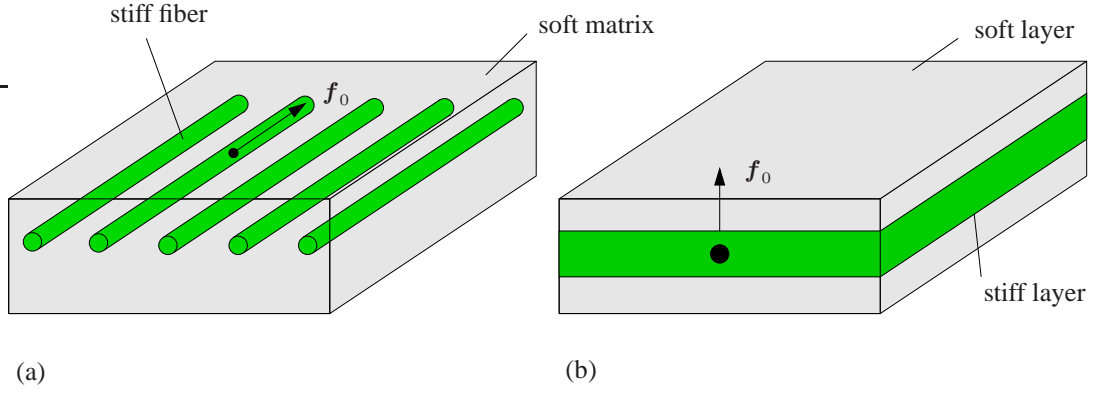
Figure 2.3: Transverse anisotropy: (a) stiff fibers embedded in soft matrix, (b) composite laminate consisting of stiff and soft layers

The isochoric part of free energy function is included into formulation at Gauss quadrature points while the volumetric and anisotropic parts which constrain quasi-incompressible and quasi-inextensible behavior will take part in the formulation at element level.

Furthermore, the Kirchoff stress expression is divided into three parts similar to the free energy function (2.16) as

$$\boldsymbol{\tau} := 2\partial_{\boldsymbol{g}}\psi = \boldsymbol{\tau}^{vol} + \boldsymbol{\tau}^{iso} + \boldsymbol{\tau}^{ani}, \tag{2.25}$$

which are isotropic parts (volumetric and isochoric parts) and anisotropic part.

The spatial elasticity moduli builds the relation between Lie derivative or Oldroyd rate of the Kirchhoff stresses and the Lie derivative of the spatial metric $\boldsymbol{g}$ via

$$\pounds_v\boldsymbol{\tau} = \mathbb{C} : \pounds_v\boldsymbol{g}/2, \tag{2.26}$$

where $\pounds_v\boldsymbol{g}$ is equal to the symmetric rate of deformation tensor as

$$\pounds_v\boldsymbol{g} = (\boldsymbol{g}\boldsymbol{l} + \boldsymbol{l}^T\boldsymbol{g}). \tag{2.27}$$

Note that $\boldsymbol{l} = \dot{\boldsymbol{F}}\boldsymbol{F}^{-1}$ is the spatial velocity gradient.

After these definitions, the Eulerian moduli expression can be also divided into volumetric, isochoric and anisotropic parts, respectively.

$$\mathbb{C} := 4\partial^2_{gg}\psi(g; F, f_0) = \mathbb{C}^{vol} + \mathbb{C}^{iso} + \mathbb{C}^{ani} \tag{2.28}$$

Then, these volumetric, isochoric and anisotropic parts of the stress and the Eulerian moduli will be defined, respectively. Firstly, the volumetric part of the Kirchoff stress expression is

$$\boldsymbol{\tau}^{vol} = 2\partial_g\psi_{vol}(J) = p\boldsymbol{g}^{-1}, \tag{2.29}$$

where

$$p = J\psi'_{vol}(J) = \frac{\kappa}{2}(J^2 - 1). \tag{2.30}$$

The Eulerian moduli term for the volumetric part can be defined as

$$\mathbb{C}^{vol} := 4\partial^2_{gg}U(J) = (p + \hat{\kappa})\boldsymbol{g}^{-1} \otimes \boldsymbol{g}^{-1} - 2p\mathbb{I}, \tag{2.31}$$

where

$$\hat{\kappa} = J^2\psi''_{vol}(J) = \frac{\kappa}{2}(J^2 + 1). \tag{2.32}$$

The isochoric part of the Kirchoff stress can be defined as

$$\boldsymbol{\tau}^{iso} := 2\partial_g\psi_{iso}(g; F) = \bar{\boldsymbol{\tau}} : \mathbb{P}, \tag{2.33}$$

where

$$\bar{\boldsymbol{\tau}} = 2\partial_g\psi_{iso}(g; \bar{F}). \tag{2.34}$$

16

Inserting (2.22) into (2.33) results

$$\boldsymbol{\tau}^{iso} = \hat{\mu}\operatorname{dev}\bar{\boldsymbol{b}} \quad \text{with} \quad \hat{\mu} = 2\frac{\partial\psi_{iso}}{\partial\bar{I}_1} = 2\left(c_1\right). \tag{2.35}$$

In equation 2.35, $\bar{\boldsymbol{b}}$ is the unimodular part of the Finger tensor which can be defined as

$$\bar{\boldsymbol{b}} = J^{-2/3}\boldsymbol{b}. \tag{2.36}$$

Isochoric part of the Eulerian moduli can be expressed as

$$\begin{aligned}
\mathbb{C}^{iso} \quad &:= \quad 4\partial^2_{\boldsymbol{gg}}\psi_{iso}(\boldsymbol{g};\boldsymbol{F}) \\
&= \quad \mathbb{P}:\left[\bar{\mathbb{C}} + \frac{2}{3}(\bar{\boldsymbol{\tau}}:\boldsymbol{g})\mathbb{I} - \tfrac{2}{3}(\bar{\boldsymbol{\tau}}\otimes\boldsymbol{g}^{-1} + \boldsymbol{g}^{-1}\otimes\bar{\boldsymbol{\tau}})\right]:\mathbb{P}^{\mathrm{T}},
\end{aligned} \tag{2.37}$$

where $\mathbb{P}^{ab}_{cd}$ is the fourth-order deviatoric projection tensor which can be expressed as

$$\mathbb{P}^{ab}_{cd} = [\delta^a_c\delta^b_d + \delta^a_d\delta^b_c]/2 - \delta^{ab}\delta_{cd}/3. \tag{2.38}$$

Also,

$$\bar{\boldsymbol{\tau}} = 2\partial_{\boldsymbol{g}}\psi_{iso}(\boldsymbol{g};\bar{\boldsymbol{F}}) \quad \text{and} \quad \bar{\mathbb{C}} := 4\partial^2_{\boldsymbol{gg}}\psi_{iso}(\boldsymbol{g};\bar{\boldsymbol{F}}) \tag{2.39}$$

are the Kirchoff stress and the Eulerian moduli related with the unimodular part of the deformation gradient. Inserting (2.22) into (2.39)$_1$, and (2.39)$_2$ into (2.22), results in

$$\bar{\boldsymbol{\tau}} = \hat{\mu}\bar{\boldsymbol{b}} \quad \text{and} \quad \bar{\mathbb{C}} = \hat{\mu}'\bar{\boldsymbol{b}}\otimes\bar{\boldsymbol{b}} \quad \text{with} \quad \hat{\mu}' = 0. \tag{2.40}$$

Finally, anisotropic part of the Kirchhoff stress can be defined as

$$\boldsymbol{\tau}^{ani} = 2\partial_{\boldsymbol{g}}\psi_{ani}(\boldsymbol{g};\boldsymbol{F},\boldsymbol{f}_0) = 2k_1\langle I_4 - 1\rangle\exp[k_2\langle I_4 - 1\rangle^2]\boldsymbol{f}\otimes\boldsymbol{f}. \tag{2.41}$$

17

Moreover, the anisotropic part of the Eulerian moduli can be written as

$$
\begin{aligned}
\mathbb{C}^{ani} &= 4\partial^2_{\boldsymbol{gg}}\psi_{ani}(\boldsymbol{g}; \boldsymbol{F}, \boldsymbol{f}_0) \\
&= 4k_1(1 + 2k_2\langle I_4 - 1\rangle^2)\exp[k_2\langle I_4 - 1\rangle^2]\boldsymbol{f} \otimes \boldsymbol{f} \otimes \boldsymbol{f} \otimes \boldsymbol{f}
\end{aligned}
\tag{2.42}
$$

2.2 Variational formulation for an anisotropic and incompressible continuum

2.2.1 Variational formulation for finite elasticity

Potential functional for *finite elasticity* can be expressed in the form

$$
\hat{\Pi}(\boldsymbol{\varphi}, t) = \hat{\Pi}^{int}(\boldsymbol{\varphi}, t) - \hat{\Pi}^{ext}(\boldsymbol{\varphi}, t)\,,
\tag{2.43}
$$

where

$$
\hat{\Pi}^{int}(\boldsymbol{\varphi}, t) = \int_{\mathscr{B}} \psi(\boldsymbol{g}, \boldsymbol{F})\, dV,
\tag{2.44}
$$

$$
\hat{\Pi}^{ext}(\boldsymbol{\varphi}) = \int_{\mathscr{B}} \boldsymbol{\varphi} \cdot \rho_0\bar{\boldsymbol{\gamma}}\, dV + \int_{\partial\mathscr{B}_t} \boldsymbol{\varphi} \cdot \bar{\boldsymbol{T}}\, dA\,,
\tag{2.45}
$$

where $\hat{\Pi}^{int}(\boldsymbol{\varphi})$ is the energy stored in the body while $\hat{\Pi}^{ext}(\boldsymbol{\varphi})$ is the work done by external forces. Also, ρ_0, $\bar{\boldsymbol{\gamma}}$, $\bar{\boldsymbol{T}}$ and $\psi(\boldsymbol{g}, \boldsymbol{F})$ are the density, prescribed body force, surface traction and volume specific free energy, respectively. The boundary value problem leading to finite elasticity is generated from the elastic potential by the *principle of minimum potential energy* in the variational form

$$
\boldsymbol{\varphi}_t = \text{Arg}\left\{\inf_{\boldsymbol{\varphi}_t \in \mathscr{W}} \hat{\Pi}(\boldsymbol{\varphi}, t)\right\}
\tag{2.46}
$$

restrained by Dirichlet-type boundary condition

$$
\mathscr{W} = \{\boldsymbol{\varphi}_t \mid \boldsymbol{\varphi}_t \in \mathscr{B} \quad \wedge \quad \boldsymbol{\varphi}_t = \bar{\boldsymbol{\varphi}} \quad \text{on} \quad \partial\mathscr{B}_u\}\,.
\tag{2.47}
$$

18

The variation of (2.46) along with localization theorem results in the *Euler–Lagrange equation* by using the stationary behavior of the potential $\hat{\Pi}(\boldsymbol{\varphi}, t)$ as

$$J \operatorname{div}[J^{-1}\boldsymbol{\tau}] + \rho_0 \bar{\boldsymbol{\gamma}} = 0, \tag{2.48}$$

which is the balance of linear momentum for quasi-static problems in domain $\mathscr{B}$ along with Neumann-type boundary condition

$$\boldsymbol{P} \cdot \boldsymbol{N} = \boldsymbol{\tau} \cdot \boldsymbol{n} = \bar{\boldsymbol{T}} \qquad \text{on} \qquad \partial \mathscr{B}_t, \tag{2.49}$$

where we have made use of the identity

$$J\boldsymbol{F}^{-T}\boldsymbol{N} \, dA = \boldsymbol{n} \, da, \tag{2.50}$$

which is also known as *Nanson's formula*. Therein, $\bar{\boldsymbol{T}} = J\boldsymbol{t}$ is the scaled traction vector.

The *Q1 element formulation* is derived by applying the consistent linearization of the weak form obtained as the first variation of (2.46). The weak form can be alternatively obtained from the momentum balance equation (2.48) by Galerkin's procedure.

2.2.2 A mixed variational formulation for a quasi-incompressible and quasi-inextensible continuum

Two penalty terms can be added to the minimization problem (2.46) to constrain the quasi-incompressible and quasi-inextensible behavior with the decomposed representation (2.16).

$$\hat{\Pi}(\boldsymbol{\varphi}, p, \theta, s, \lambda) := \int_{\mathscr{B}} \pi^*(\boldsymbol{\varphi}, p, \theta, s, \lambda) \, dV - \hat{\Pi}^{ext}(\boldsymbol{\varphi}, t). \tag{2.51}$$

The mixed potential density ($\pi^*(\boldsymbol{\varphi}, p, \theta, s, \lambda)$) introduced in equation (2.51) can be defines as

19

$$\pi^*(\boldsymbol{\varphi}, p, \theta, s, \lambda) = \psi_{iso}(\boldsymbol{g}, \bar{\boldsymbol{F}}) + \underbrace{p(J - \theta) + \psi_{vol}(\theta)}_{\text{volumetric constraint}} + \underbrace{s(I_4 - \lambda) + \psi_{ani}(\lambda)}_{\text{inextensibility constraint}}. \quad (2.52)$$

In equation (2.52), p and s are penalty parameters used with the kinematic quantities θ and λ, respectively.

Then, the motion of the body restrained by incompressibility and inextensibility constraints is defined by using the *mixed saddle point principle*

$$\{\boldsymbol{\varphi}_t, \theta, p, \lambda, s\} = \text{Arg} \left\{ \inf_{\boldsymbol{\varphi}_t \in \mathscr{W}} \inf_{\theta} \inf_{\lambda} \sup_{p} \sup_{s} \hat{\Pi}(\boldsymbol{\varphi}, t) \right\} \quad (2.53)$$

subjected to the boundary conditions

$$\mathscr{W} = \{\boldsymbol{\varphi}_t \mid \boldsymbol{\varphi}_t \in \mathscr{B} \quad \wedge \quad \boldsymbol{\varphi}_t = \bar{\boldsymbol{\varphi}} \quad \text{on} \quad \partial \mathscr{B}_u\}. \quad (2.54)$$

After these definitions, variations of (2.51) with respect to $\boldsymbol{\varphi}$, p, θ, s and λ are taken and this results in the weak form;

$$\begin{aligned}
\delta_{\boldsymbol{\varphi}} \hat{\Pi}(\boldsymbol{\varphi}, p, \theta, s, \lambda) &= \int_{\mathscr{B}} \left\{ (\boldsymbol{\tau}^{iso} + pJ\boldsymbol{g}^{-1} + 2s\boldsymbol{f} \otimes \boldsymbol{f}) : \frac{1}{2} \boldsymbol{\pounds}_{\delta\boldsymbol{\varphi}} \boldsymbol{g} \right\} dV \\
&\quad - \delta \hat{\Pi}^{ext}(\boldsymbol{\varphi}) = 0, \\
\delta_p \hat{\Pi}(\boldsymbol{\varphi}, p, \theta, s, \lambda) &= \int_{\mathscr{B}} \delta p \, (J - \theta) \, dV = 0, \\
\delta_{\theta} \hat{\Pi}(\boldsymbol{\varphi}, p, \theta, s, \lambda) &= \int_{\mathscr{B}} \delta\theta \, (\psi'_{vol}(\theta) - p) \, dV = 0, \\
\delta_s \hat{\Pi}(\boldsymbol{\varphi}, p, \theta, s, \lambda) &= \int_{\mathscr{B}} \delta s \, (I_4 - \lambda) \, dV = 0, \\
\delta_{\lambda} \hat{\Pi}(\boldsymbol{\varphi}, p, \theta, s, \lambda) &= \int_{\mathscr{B}} \delta\lambda \, (\psi'_{ani}(\lambda) - s) \, dV = 0.
\end{aligned} \quad (2.55)$$

By using these weak form equations (2.55), mixed finite element method can be built. In equation (2.55.1), $\boldsymbol{\pounds}_{\delta\boldsymbol{\varphi}} \boldsymbol{g}$ is the Lie derivative of the current metric along the vari-

ation $\delta\boldsymbol{\varphi}$. Taking the variation of the potential density (2.52), *Euler–Lagrange equations* of the mixed variational principle can be written as

$$
\begin{aligned}
1. \quad & J\operatorname{div}[J^{-1}\boldsymbol{\tau}] + \rho_0\bar{\boldsymbol{\gamma}} = 0 \\
2. \quad & J - \theta && = 0 \\
3. \quad & \psi'_{vol}(\theta) - p && = 0 \\
4. \quad & I_4 - \lambda && = 0 \\
5. \quad & \psi'_{ani}(\lambda) - s && = 0
\end{aligned}
\tag{2.56}
$$

throughout the Neumann-type boundary conditions $\mathscr{W}_t = \{\boldsymbol{\sigma}\cdot\boldsymbol{n} = \boldsymbol{t} \quad \text{on} \quad \partial\mathscr{B}_t\}$.

2.2.3 Consistent linearization of the mixed potential

The following identity can be proven

$$
\frac{1}{2}\pounds_{\delta\varphi}\boldsymbol{g} = \operatorname{sym}\left(\boldsymbol{g}\nabla_x\delta\boldsymbol{\varphi}\right).
\tag{2.57}
$$

Therefore, the term $\frac{1}{2}\pounds_{\delta\varphi}\boldsymbol{g}$ can be replaced with $\operatorname{sym}\left(\boldsymbol{g}\nabla_x\delta\boldsymbol{\varphi}\right)$ in equation (2.55.1).

Moreover, there is a nonlinearity in equation (2.55.1) in terms of $\boldsymbol{\varphi}$. Also, equations (2.55.2-5) behave as additional constraints on (2.55.1). Equation (2.55.1) can be linearized consistently around $\boldsymbol{\varphi}$ as

$$
\begin{aligned}
D\delta_\varphi\hat{\Pi}\cdot\Delta\boldsymbol{\varphi} = {}& \int_{\mathscr{B}} \boldsymbol{g}\nabla_x\delta\boldsymbol{\varphi} : \left\{\nabla_x\Delta\boldsymbol{\varphi}\left(\boldsymbol{\tau}^{iso} + pJ\boldsymbol{g}^{-1} + 2s\boldsymbol{f}\otimes\boldsymbol{f}\right)\right\}\ dV \\
& + \int_{\mathscr{B}} \boldsymbol{g}\nabla_x\delta\boldsymbol{\varphi} : \left\{pJ\mathbb{V} + \mathbb{C}^{iso}\right\} : \boldsymbol{g}\nabla_x\Delta\boldsymbol{\varphi}\ dV \\
& + \int_{\mathscr{B}} \boldsymbol{g}\nabla_x\delta\boldsymbol{\varphi} : J\Delta p\boldsymbol{g}^{-1}\ dV. \\
& + \int_{\mathscr{B}} \boldsymbol{g}\nabla_x\delta\boldsymbol{\varphi} : 2\Delta s\boldsymbol{f}\otimes\boldsymbol{f}\ dV
\end{aligned}
\tag{2.58}
$$

with the following description

$$
\mathbb{V} = \boldsymbol{g}^{-1}\otimes\boldsymbol{g}^{-1} - 2\mathbb{I}_{\boldsymbol{g}^{-1}},
\tag{2.59}
$$

where $\mathbb{I}_{\boldsymbol{g}^{-1}}{}^{abcd}$ is the fourth-order symmetric identity map which is defined as

$$\mathbb{I}_{\boldsymbol{g}^{-1}}{}^{abcd} = (\delta^{ac}\delta^{bd} + \delta^{ad}\delta^{bc})/2. \tag{2.60}$$

Equation (2.55.1) stands for the balance of linear momentum and equations (2.55.2-5) are the constraint equations driving incompressible and inextensible behavior for quasi-static problems. The equations (2.55.2-5) will be enforced weakly within subdomains $\mathscr{B}_e$ such that $\mathscr{B}_0 \approx \bigcup_{e=1}^{n_e} \mathscr{B}_e$ where n_e denotes the number of the subdomains.

The kinematical variable θ and the penalty parameter p can be derived with equations (2.55.2) and (2.55.3) within the subdomain $\mathscr{B}_e$ as

$$\bar{\theta} = \frac{1}{V^e} \int_{\mathscr{B}_e} J \, dV \,, \tag{2.61}$$

$$\bar{p} = \frac{1}{V^e} \int_{\mathscr{B}_e} \psi'_{vol}(\theta) \, dV = \psi'_{vol}(\bar{\theta}). \tag{2.62}$$

Equations (2.61) and (2.62) result in a constant values for the $\bar{\theta}$ and $\bar{p}$ which can be explained as the mean dilatation and the mean pressure over the element domain. The incremental forms of the mean pressure $\bar{p}$ and the mean dilatation $\bar{\theta}$ can be derived as

$$\Delta\bar{p} = \psi''_{vol}(\bar{\theta})\Delta\bar{\theta}, \tag{2.63}$$

where

$$\Delta\bar{\theta} = \frac{1}{V^e} \int_{\mathscr{B}_e} J\boldsymbol{g}^{-1} : \boldsymbol{g}\nabla_x\Delta\boldsymbol{\varphi} \, dV. \tag{2.64}$$

By using the same discretization in the derivation of $\bar{\theta}$ and $\bar{p}$, the kinematical variable λ and the penalty parameter s can be derived with (2.55.4) and (2.55.5) within the subdomain $\mathscr{B}_e$ as

$$\bar{\lambda} = \frac{1}{V^e} \int_{\mathscr{B}_e} I_4 \, dV, \tag{2.65}$$

22

$$\bar{s} = \frac{1}{V^e} \int_{\mathcal{B}_e} \psi'_{ani}(\lambda) \, dV \approx \psi'_{ani}(\bar{\lambda}). \tag{2.66}$$

Equations (2.65) and (2.66) result in a constant values for $\bar{\lambda}$ and $\bar{s}$ which can be explained as the mean fiber stretch and the mean fiber stress over the element domain. The incremental forms of the mean fiber stretch and mean fiber stress can be defined as

$$\Delta\bar{s} = \psi''_{ani}(\bar{\lambda})\Delta\bar{\lambda}, \tag{2.67}$$

where

$$\Delta\bar{\lambda} = \frac{1}{V^e} \int_{\mathcal{B}_e} 2\boldsymbol{f} \otimes \boldsymbol{f} : \boldsymbol{g}\nabla_x\Delta\boldsymbol{\varphi} \, dV. \tag{2.68}$$

The stresses and the moduli equations can be rederived as

$$\hat{\boldsymbol{\tau}} = \boldsymbol{\tau}^{iso} + \bar{p}J\boldsymbol{g}^{-1} + 2\bar{s}\boldsymbol{f} \otimes \boldsymbol{f}, \tag{2.69}$$

$$\hat{\mathbb{C}} = \bar{p}J\mathbb{V} + \mathbb{C}^{iso}. \tag{2.70}$$

Finally, by applying the symmetry of $\hat{\boldsymbol{\tau}}$ and $\hat{\mathbb{C}}$ and substituting equations (2.63, 2.64, 2.67, 2.68) and (2.69) into equation (2.58), final equation for the linearized term can be written as

$$\begin{aligned}
D\delta_\varphi\hat{\Pi} \cdot \Delta\boldsymbol{\varphi} &= \underset{e=1}{\overset{n}{\mathsf{A}}} \left\{ \int_{\mathcal{B}_e} \boldsymbol{g}\nabla_x\delta\boldsymbol{\varphi} : \nabla_x\Delta\boldsymbol{\varphi} \, \hat{\boldsymbol{\tau}} \, dV \right. \\
&\quad + \int_{\mathcal{B}_e} \boldsymbol{g}\nabla_x\delta\boldsymbol{\varphi} : \hat{\mathbb{C}} : \boldsymbol{g}\nabla_x\Delta\boldsymbol{\varphi} \, dV \\
&\quad + \int_{\mathcal{B}_e} J\boldsymbol{g}\nabla_x\delta\boldsymbol{\varphi} : \boldsymbol{g}^{-1} \, dV \, \psi''_{vol}(\bar{\theta}) \frac{1}{V^e} \int_{\mathcal{B}_e} J\boldsymbol{g}\nabla_x\Delta\boldsymbol{\varphi} : \boldsymbol{g}^{-1} \, dV \\
&\quad \left. + \int_{\mathcal{B}_e} \boldsymbol{g}\nabla_x\delta\boldsymbol{\varphi} : 2\boldsymbol{f} \otimes \boldsymbol{f} \, dV \, \psi''_{ani}(\bar{\lambda}) \frac{1}{V^e} \int_{\mathcal{B}_e} \boldsymbol{g}\nabla_x\Delta\boldsymbol{\varphi} : 2\boldsymbol{f} \otimes \boldsymbol{f} \, dV \right\} \\
&\quad\quad\quad\quad\quad\quad\quad\quad\quad\quad\quad\quad\quad\quad\quad\quad\quad\quad\quad\quad\quad\quad\quad\quad\quad\quad\quad (2.71)
\end{aligned}$$

23

2.3 Finite element formulation
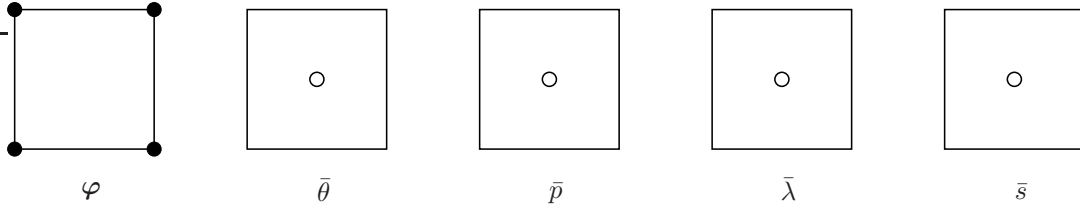
Figure 2.4: *Q1P0F0* mixed finite element formulation sketch for quasi-incompressible and quasi-inextensible hyperelasticity.

2.3.1 Element discretization

In this section, spatial discretization of variables will be conducted. The aim of this step is to get algebraic correspondents of the residual equation (2.55.1) and to create the element matrices from linearized equation (2.71). In the element phase, the introduced mean values $\bar{p}$, $\bar{\theta}$, $\bar{s}$ and $\bar{\lambda}$ are kept constant whereas the trilinear interpolation is applied for field φ as it is shown in Figure 2.4. Figure 2.4 is given in two dimensional form for clarity. After that, interpolation of the field variables and the associated weight functions on each element domain is conducted by defining discrete nodal values and $\mathscr{C}^0$-continuous shape functions as

$$\varphi^h = \sum_{I=1}^{n_{en}} \mathcal{N}^I \, \hat{\boldsymbol{x}}_I, \tag{2.72}$$

$$\delta\varphi^h = \sum_{I=1}^{n_{en}} \mathcal{N}^I \, \delta\hat{\boldsymbol{x}}_I, \tag{2.73}$$

$$\Delta\varphi^h = \sum_{I=1}^{n_{en}} \mathcal{N}^I \, \Delta\hat{\boldsymbol{x}}_I, \tag{2.74}$$

where n_{en} means node number per element. The spatial gradient of the weight function and incremental field can be derived by using discretization in equations (2.73) and (2.74) as

24

$$\nabla_x(\delta\boldsymbol{\varphi}^h) = \sum_{I=1}^{n_{en}} \delta\hat{\boldsymbol{x}}_I \otimes \nabla_x\mathcal{N}^I, \tag{2.75}$$

$$\nabla_x\Delta\boldsymbol{\varphi}^h = \sum_{I=1}^{n_{en}} \Delta\hat{\boldsymbol{x}}_I \otimes \nabla_x\mathcal{N}^I. \tag{2.76}$$

By inserting equations (2.72, 2.73, 2.74 2.75, 2.76) into (2.55), we can obtain the residual vector in discrete form as

$$\mathbb{R}^\varphi = \mathop{\textsf{A}}_{e=1}^{n_{el}} \sum_{I=1}^{n_{en}} \int_{\mathscr{B}_e^h} \left[\nabla_x\mathcal{N}^I \cdot \hat{\boldsymbol{\tau}} - \mathcal{N}^I\rho_0\bar{\boldsymbol{\gamma}}\right] \, dV - \mathop{\textsf{A}}_{e=1}^{n_{el}^s} \sum_{I=1}^{n_{en}^s} \int_{\partial\mathscr{S}_t^e} \mathcal{N}^I \bar{\boldsymbol{T}} \, dA = \boldsymbol{0}. \tag{2.77}$$

In equation (2.77), $\textsf{A}$ stands for an operator which is used for the assembly of element contributions at the local element nodes $I = 1, \ldots, n_{en}$ over n_{el} subdomains.

Then, linearization of the residual expression can be defined as

$$\text{Lin}\,\mathbb{R}^\varphi = \mathbb{R}^\varphi + \frac{\partial\mathbb{R}^\varphi}{\partial\mathbb{U}}\Delta\mathbb{U}, \tag{2.78}$$

where

$$\mathbb{U} = \mathop{\textsf{A}}_{e=1}^{n_{el}} \hat{\boldsymbol{x}}^h. \tag{2.79}$$

Stiffness matrix can be obtained by inserting (2.72, 2.73, 2.74 2.75, 2.76) into (2.71) as

$$\mathbb{K} = \frac{\partial\mathbb{R}^\varphi}{\partial\mathbb{U}} = \mathop{\textsf{A}}_{e=1}^{n_{el}} \mathbb{K}_{el}, \tag{2.80}$$

where $\mathbb{K}_{el}$ is the element stiffness matrix. It can be divided into material, geometric, volumetric and anisotropic contributions as

$$\mathbb{K}_{el} = \mathbb{K}_{el}^{mat} + \mathbb{K}_{el}^{geo} + \mathbb{K}_{el}^{vol} + \mathbb{K}_{el}^{ani}. \tag{2.81}$$

25

Also, elemental average quantities can be expressed as;

$$\nabla_x \bar{\mathcal{N}}^I = \int_{\mathcal{B}_{el}^h} J \, \nabla_x \mathcal{N}^I \, dV \, , \tag{2.82}$$

$$\nabla_x \bar{\mathcal{F}}^I = \int_{\mathcal{B}_{el}^h} \nabla_x \mathcal{N}^I : \boldsymbol{f} \otimes \boldsymbol{f} \, dV. \tag{2.83}$$

Stiffness contributions can be derived by using elemental average quantities as

$$\mathbb{K}_{el}^{mat \, IJ} = \int_{\mathcal{B}_{el}^h} \nabla_x^T \mathcal{N}^I \cdot \hat{\mathbb{C}} \cdot \nabla_x \mathcal{N}^J \, dV \, , \tag{2.84}$$

$$\mathbb{K}_{el}^{vol \, IJ} = \nabla_x^T \bar{\mathcal{N}}^I \, \frac{\psi_{vol}''(\bar{\theta})}{V_e} \, \nabla_x \bar{\mathcal{N}}^J \, , \tag{2.85}$$

$$\mathbb{K}_{el}^{geo \, IJ} = \int_{\mathcal{B}_{el}^h} \nabla_x \mathcal{N}^I \cdot \hat{\boldsymbol{\tau}} \cdot \nabla_x \mathcal{N}^J \, dV \, , \tag{2.86}$$

$$\mathbb{K}_{el}^{ani \, IJ} = \nabla_x^T \bar{\mathcal{F}}^I \, \frac{\psi_{ani}''(\bar{\lambda})}{V_e} \, \nabla_x \bar{\mathcal{F}}^J \, . \tag{2.87}$$

An 8 noded brick element will be used in the upcoming representative examples. Therefore, the shape functions and corresponding nodal values for this element can be introduced as

$$\mathcal{N}^I(\boldsymbol{\xi}) = \frac{1}{8}(1 + \xi_1 \xi_1^I)(1 + \xi_2 \xi_2^I)(1 + \xi_3 \xi_3^I), \tag{2.88}$$

$$
\begin{aligned}
\xi_1^I &= [-1 \quad +1 \quad +1 \quad -1 \quad -1 \quad +1 \quad +1 \quad -1] \\
\xi_2^I &= [-1 \quad -1 \quad +1 \quad +1 \quad -1 \quad -1 \quad +1 \quad +1] \\
\xi_3^I &= [-1 \quad -1 \quad -1 \quad -1 \quad +1 \quad +1 \quad +1 \quad +1]
\end{aligned} \tag{2.89}
$$

26
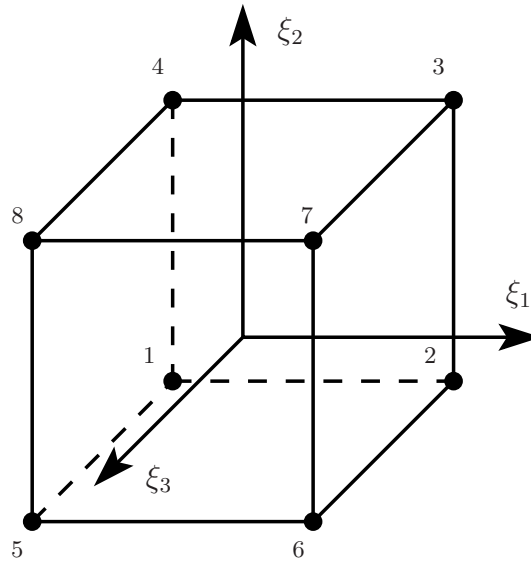
Figure 2.5: Bi-unit cube in the parameter space. Local coordinates are defined by $\boldsymbol{\xi} \in \mathcal{A}$, where $\mathcal{A} := \{\boldsymbol{\xi} \in \mathbb{R}^3 \mid -1 \leq \xi_i \leq +1 \; ; \; i = 1, 3\}$.

This shape functions are for a cubic structure in the parametric space as shown in Figure 2.5. Flowchart for the computation of the element stiffness matrix can be seen more clearly in Table 2.1.

Table 2.1: Calculation of *Q1P0F0* element stiffness matrix [12]

---

a) Volumetric and anisotropic contributions of stiffness matrix:

Mean parameters, $\bar{\theta}$, $\bar{p}$, $\bar{\lambda}$ and $\bar{s}$, will be calculated.

$\Big\{$ LOOP $[\alpha = 1, 8]$ Given: placement $\hat{\boldsymbol{x}}^h = \hat{\boldsymbol{u}}^h + \hat{\boldsymbol{X}}^h$, shape functions $\boldsymbol{\mathcal{N}}(\boldsymbol{\xi}) := \mathcal{N}^I(\boldsymbol{\xi})$

$\qquad\qquad\qquad$ Set: $V^e = v^e = 0$ $\bar{\lambda} = 0$

1. Calculate shape function, derivative of the shape function in parametric space and transformation map at $\boldsymbol{\xi}(\alpha)$

$$\boldsymbol{\mathcal{N}}(\boldsymbol{\xi}), \quad \nabla_\xi \boldsymbol{\mathcal{N}}(\boldsymbol{\xi}) \quad \text{and} \quad \boldsymbol{J} = \nabla_\xi \boldsymbol{\mathcal{N}} \hat{\boldsymbol{X}}^h \quad \text{at} \quad \boldsymbol{\xi} = \boldsymbol{\xi}(\alpha)$$

2. Calculate the material and spatial derivative of shape functions, and deformation gradient

$$\nabla_X \boldsymbol{\mathcal{N}} = \nabla_\xi \boldsymbol{\mathcal{N}} \boldsymbol{J}^{-1}, \quad \boldsymbol{F} = \nabla_X \boldsymbol{\mathcal{N}} \hat{\boldsymbol{x}} \quad \text{and} \quad \nabla_x \boldsymbol{\mathcal{N}} = \nabla_X \boldsymbol{\mathcal{N}} \boldsymbol{F}^{-1}$$

3. Calculate the initial and current element volume and the integrate the fiber stretch $\boldsymbol{f} = \boldsymbol{F} \boldsymbol{f}_0$

$$V^e \leftarrow V^e + \det \boldsymbol{J} w_\alpha \qquad\qquad v^e \leftarrow v^e + \det \boldsymbol{J} \det \boldsymbol{F} w_\alpha$$

$$\lambda = \boldsymbol{f} \cdot \boldsymbol{g} \boldsymbol{f} \qquad\qquad\qquad \bar{\lambda} \leftarrow \bar{\lambda} + \lambda \det \boldsymbol{J} w_\alpha$$

4. Calculate $\nabla_x \bar{\boldsymbol{\mathcal{N}}} := \nabla_x \bar{\mathcal{N}}^I$ and $\nabla_x \bar{\boldsymbol{\mathcal{F}}} := \nabla_x \bar{\mathcal{F}}^I$

$$\nabla_x \bar{\boldsymbol{\mathcal{N}}} \leftarrow \nabla_x \bar{\boldsymbol{\mathcal{N}}} + \det \boldsymbol{J} \det \boldsymbol{F} w_\alpha \nabla_x \boldsymbol{\mathcal{N}} \qquad \nabla_x \bar{\boldsymbol{\mathcal{F}}} \leftarrow \nabla_x \bar{\boldsymbol{\mathcal{F}}} + \det \boldsymbol{J} w_\alpha \nabla_x \boldsymbol{\mathcal{N}} : \boldsymbol{f} \otimes \boldsymbol{f} \quad \Big\}$$

5. Calculate $\bar{\theta}$, $\bar{p}$, $\bar{\lambda}$ and $\bar{s}$

$$\bar{\theta} = \frac{v^e}{V^e} \qquad \bar{p} = \psi'_{vol}(\bar{\theta}) \qquad \bar{\lambda} \leftarrow \frac{\bar{\lambda}}{V^e} \qquad \bar{s} = \psi'_{ani}(\bar{\lambda})$$

6. Calculate $\boldsymbol{K}_{vol}$ and $\boldsymbol{K}_{ani}$

$$K_{vol}{}^{3(I-1)+i,\,3(J-1)+j} = (\bar{\mathcal{N}}_{,x})^I_i \frac{\psi''_{vol}(\bar{\theta})}{V^e} (\bar{\mathcal{N}}_{,x})^J_j$$

$$K_{ani}{}^{3(I-1)+i,\,3(J-1)+j} = (\bar{\mathcal{F}}_{,x})^I_i \frac{\psi''_{ani}(\bar{\lambda})}{V^e} (\bar{\mathcal{F}}_{,x})^J_j$$

b) Material and geometric part of the stiffness matrix:

$\Big\{$ LOOP $[\alpha = 1, 8]$

7. Calculate $\boldsymbol{K}_{mat}$ and $\boldsymbol{K}_{geo}$

$$K_{geo}{}^{3(I-1)+a,\,3(J-1)+a} = K_{geo} + (\mathcal{N}_{,x})^I_i (\mathcal{N}_{,x})^J_j \tau^{ij} \det \boldsymbol{J} w_\alpha$$

$$K_{mat}{}^{3(I-1)+i,\,3(J-1)+k} = K_{mat} + (\mathcal{N}_{,x})^I_j \hat{\mathbb{C}}^{ijkl} (\mathcal{N}_{,x})^J_l \det \boldsymbol{J} w_\alpha \Big\}$$

CHAPTER 3

VALIDATION OF THE MODEL

3.1 Model Description

This section contains comparison of the proposed formulation with the standard linear displacement element ($Q1$) formulation and the mean dilatation approach denoted as $Q1P0$ formulation. For this purpose, the model similar to the numerical example recently studied by Schröder et al. [51] is analyzed. A square block is fixed at top ($y = 1$) and bottom ($y = 0$) surfaces and left surface ($x = 0$) is subjected to an uniformly distributed loading q_0 which can be clearly seen from Figure 3.1. Also, the fibers are aligned $\alpha = 60°$ from the horizontal plane. The square block has unit dimensions of 1×1. The original problem is two dimensional. The current formulation is reduced to two dimensional setting by clamping the nodes against the motion in $z-$direction by applying $u_z = 0$ for all nodes. Therefore, this leads the plane-strain problem as it is studied in the reference [51].

The fiber direction $\boldsymbol{f}_0 = [0.5, \sqrt{3}/2, 0]$ is kept constant and the loading q_0 is varied as $q_0 = \{50, 100, 150, 200\}$ kPa in order to study the stability of the proposed formulation towards inextensibility limit. The specimen is monotonically loaded to via $q(t) = q_o t$. Initially, the time increment is taken as $\Delta t = 1$. If the global Newton-Raphson algorithm does not converge within 15 time steps, the time increment is decreased and the simulation is restarted from $t = 0$.

In this set of analysis, material parameters, given in Table 3.1, are kept constant. These parameters represent the media layer of the arterial wall taken from the work of Holzapfel et al. [24]. The material behavior can be seen from Figure 3.2 (a-b).
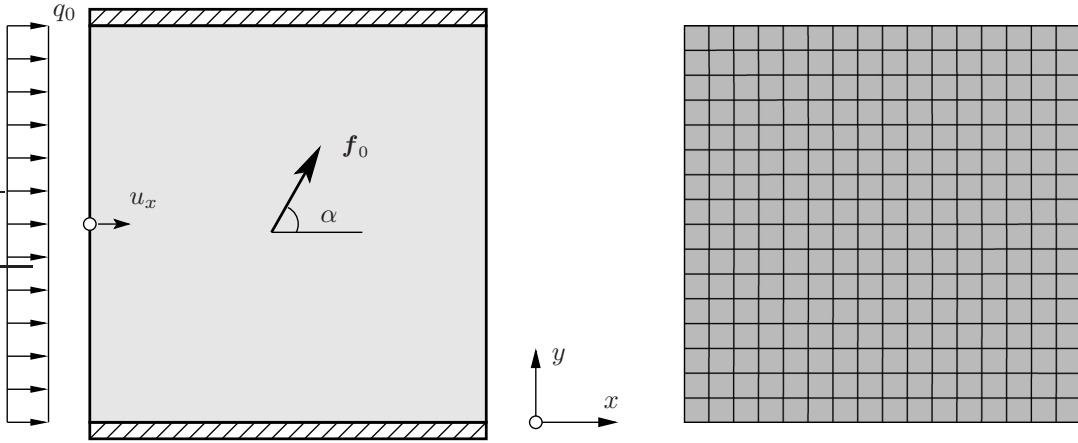
Figure 3.1: Description of the model.

Table 3.1: Material parameters.

| Parameter	Value	Unit	Parameter	Value	Unit
κ	10^4	[kPa]	$\mu = 2c_1$	27	[kPa]
k_1	0.64	[kPa]	k_2	3.54	[-]
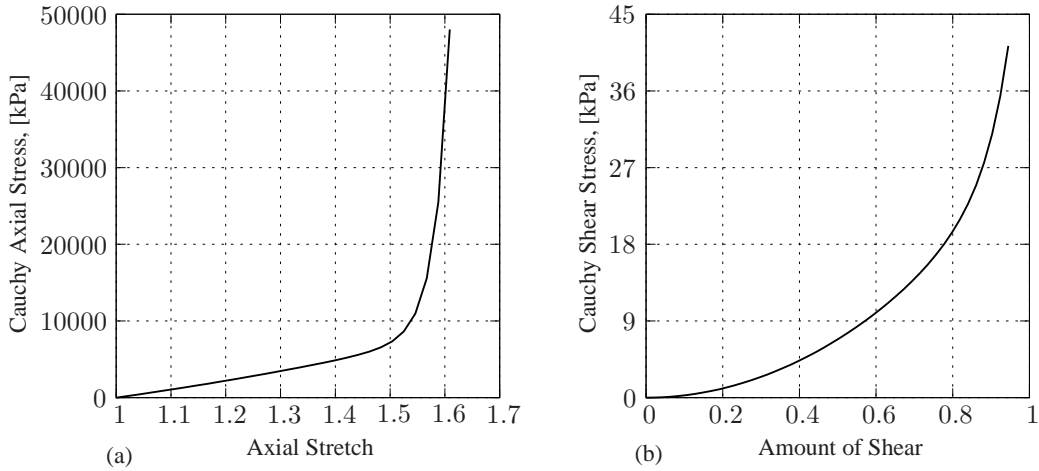
Figure 3.2: Material behavior curves of arterial wall for (a) axial stress-axial stretch under uniaxial loading and (b) out of plane shear stress-amount of shear under simple shear loading.

Figure 3.2 (a) shows the behavior of arterial wall in fiber direction under uniaxial loading while Figure 3.2 (b) shows the behavior of arterial wall in transverse direction under simple shear. When Cauchy stress results are compared, it is clearly seen that the material is much stiffer in the fiber direction with respect to transverse direction. Furthermore, Figure 3.2 (a) exhibits exponential stiffening behavior of arterial wall

30

in fiber direction. Material reaches inextensibility limit with increasing axial stretch values.

For the analysis, $n \times n$ brick elements are used and six set of mesh densities are applied where number of elements per edge are varied as $n = \{2, 4, 8, 16, 32, 64\}$.

q_0 value is increased step by step to show the convergence of the proposed formulation towards the inextensibility limit with respect to the standard linear displacement element (*Q1*) formulation and the mean dilatation approach (*Q1P0*).

3.2 Results

The results of the analyses can be seen in Figures 3.3, 3.5, 3.7, 3.9. In these figures, the left columns show the number of iteration and right columns show the horizontal displacement (u_x) for the center of the left surface, see Figure 3.1. Also, horizontal axis shows the number of elements per square block edge. As the number of the elements increases, mesh size becomes finer.
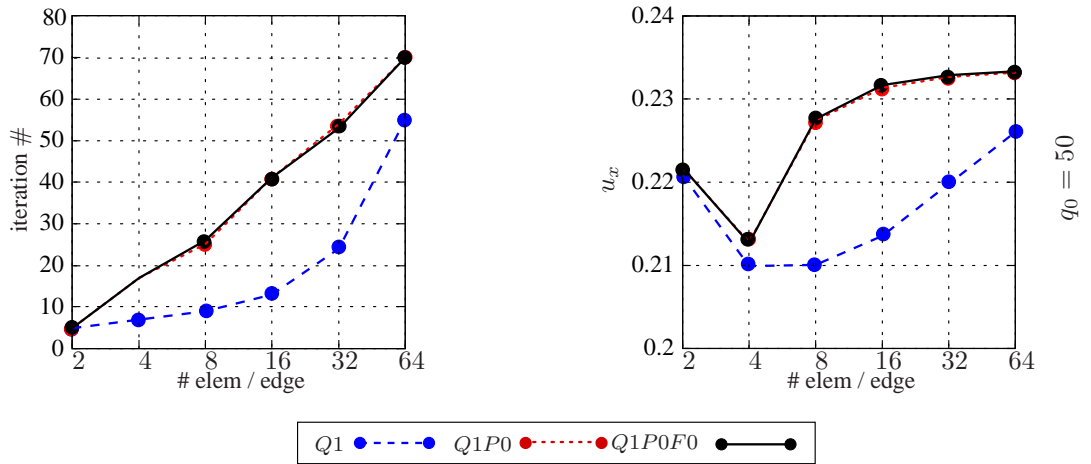

Figure 3.3: Comparison of the $Q1$, $Q1P0$ and $Q1P0F0$ element formulations for pressure value $q_0 = 50$ kPa.

Figure 3.3 shows the results of the analyses conducted at $q_0 = 50$ kPa. As it can be seen from Figure 3.3, *Q1* formulation is not convergent with the increased mesh resolution. Moreover, mesh convergences of the *Q1P0* and *Q1P0F0* formulations are almost equal to each other. Also, Figure 3.4 shows the fiber stress results at $q_0 = 50$ kPa for a mesh size of 32 elements per edge. Fiber stress magnitudes are almost equal

31
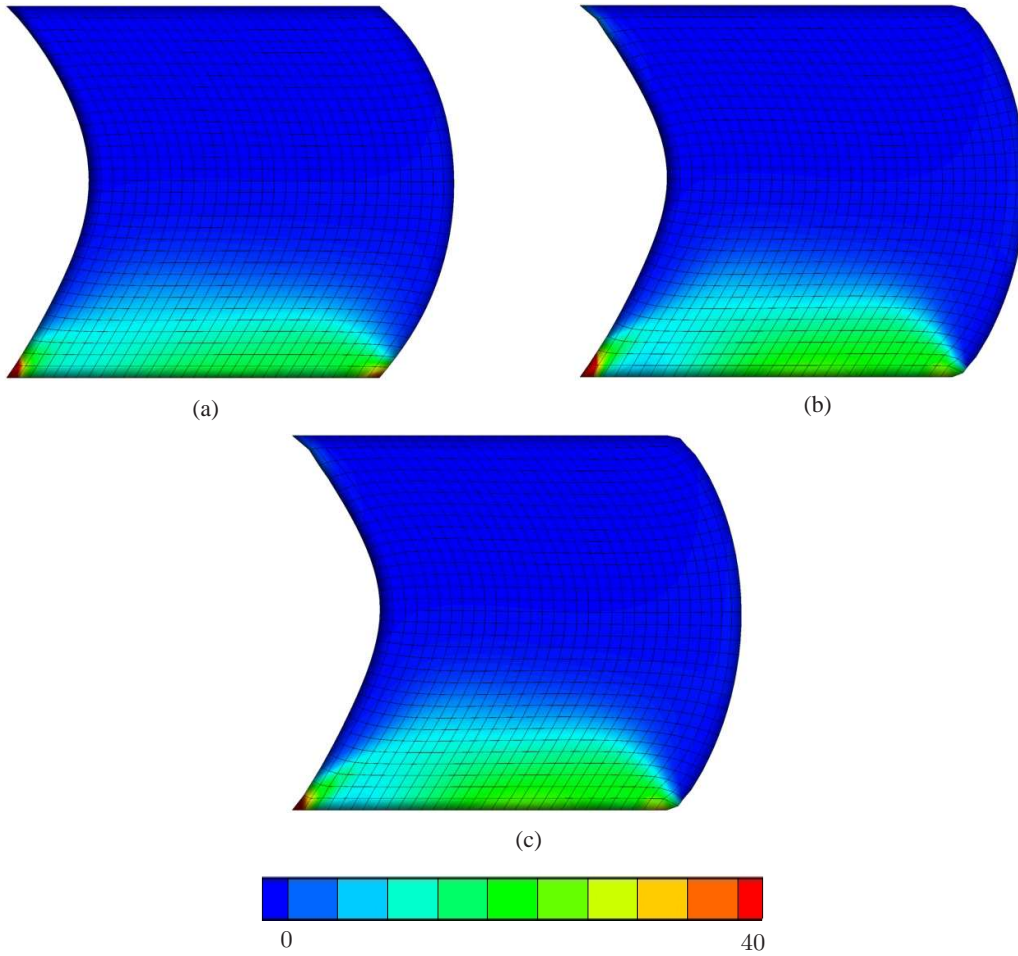
Figure 3.4: Fiber stress results for (a) $Q1$ (b) $Q1P0$ and (c) $Q1P0F0$ element formulations for pressure value $q_0 = 50$ kPa with mesh size 32 elements per edge.

for the *Q1P0F0*, *Q1* and *Q1P0* formulations.
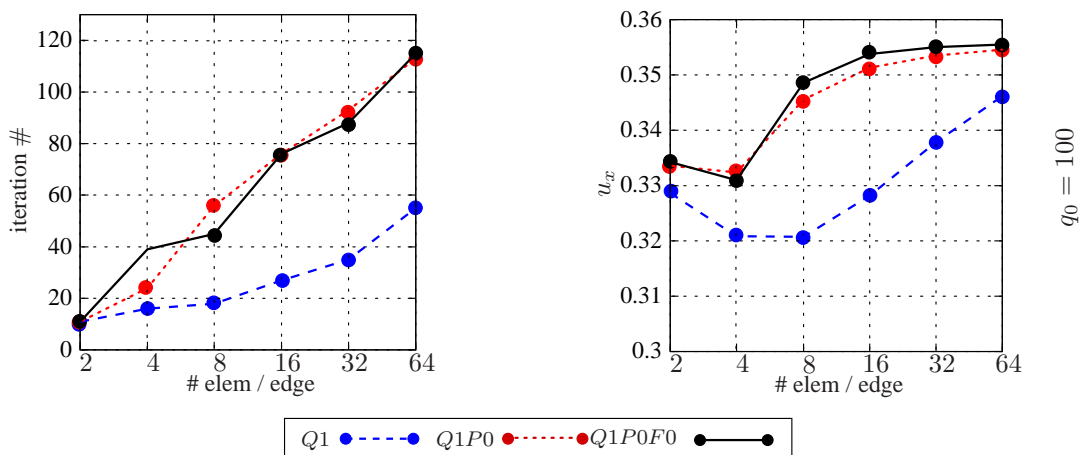
Figure 3.5: Comparison of the $Q1$, $Q1P0$ and $Q1P0F0$ element formulations for pressure value $q_0 = 100$ kPa.
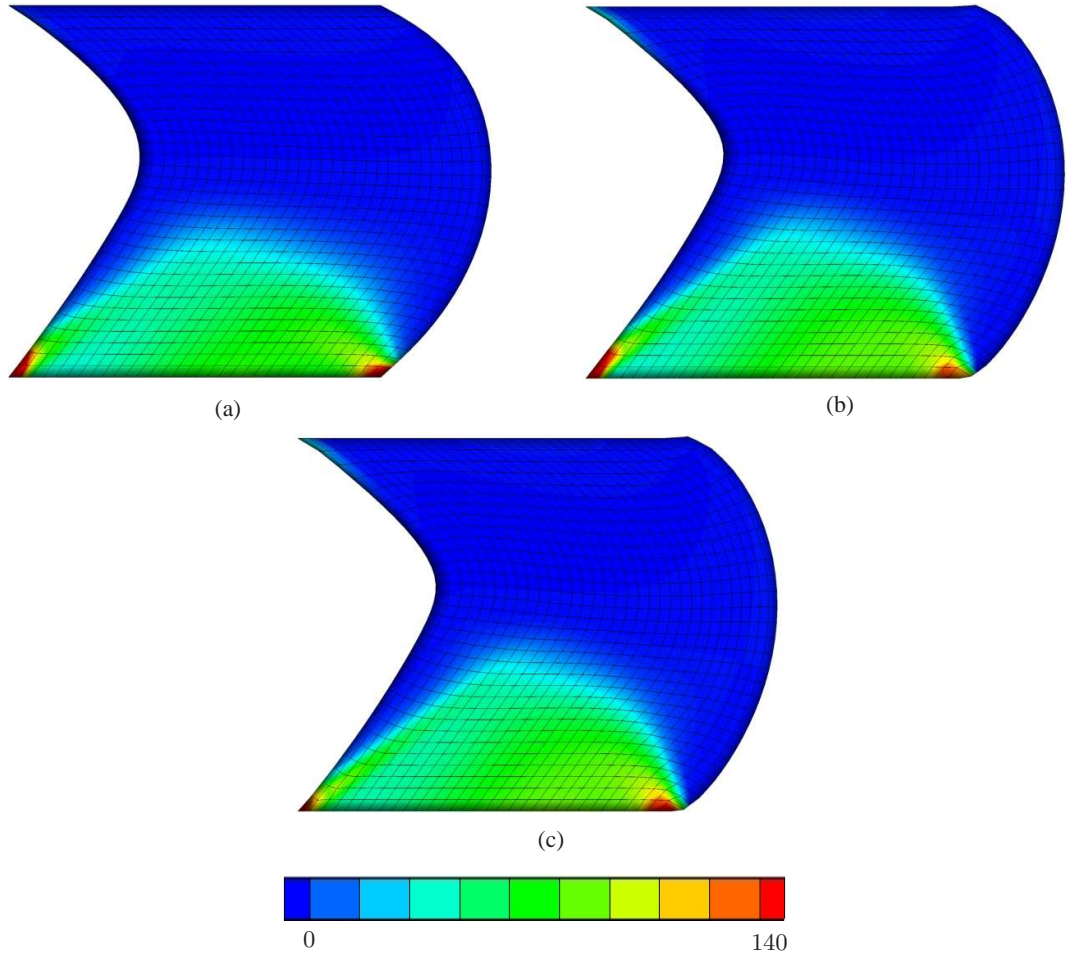
Figure 3.6: Fiber stress results for (a) $Q1$ (b) $Q1P0$ and (c) $Q1P0F0$ element formulations for pressure value $q_0 = 100$ kPa with mesh size 32 elements per edge.

Figure 3.5 shows the results of the analyses conducted at $q_0 = 100$ kPa. As it is shown in the figure 3.5, *Q1* formulation is not convergent with the increased mesh resolution. Moreover, mesh convergences of the *Q1P0* and *Q1P0F0* formulations are close to each other. Also, Figure 3.6 shows the fiber stress results at $q_0 = 100$ kPa for a mesh size of 32 elements per edge. Fiber stress magnitudes are slightly higher for the *Q1* and *Q1P0* formulations than *Q1P0F0* formulation.

Figure 3.7 shows the results of the analyses conducted at $q_0 = 150$ kPa. *Q1* formulation is not convergent with the increased mesh resolution. Mesh convergence of the mid-displacement for increasing mesh density for *Q1P0F0* formulation is better than *Q1P0* formulation. Also, Figure 3.8 shows the fiber stress results at $q_0 = 150$ kPa for a mesh size of 32 elements per edge. Fiber stress values are higher for the *Q1* and *Q1P0* formulations than *Q1P0F0* formulation.

33
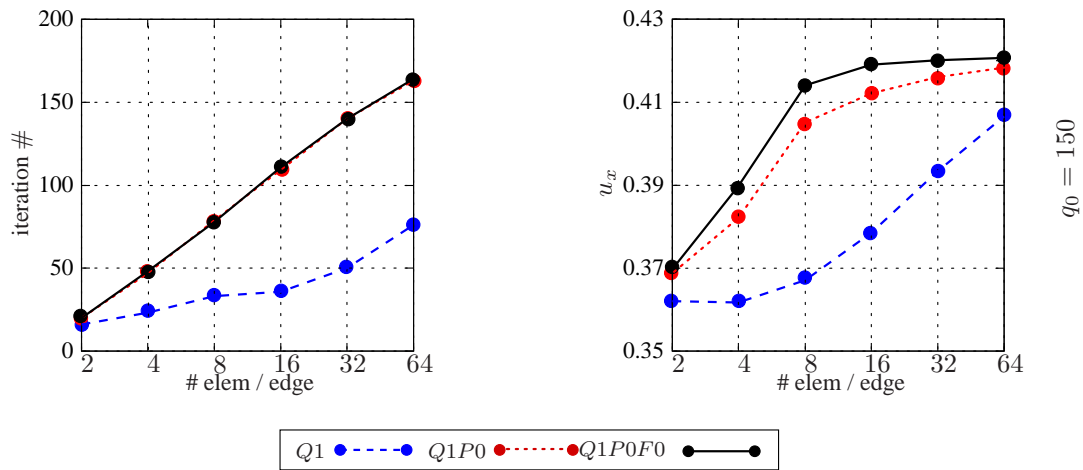
Figure 3.7: Comparison of the $Q1$, $Q1P0$ and $Q1P0F0$ element formulations for pressure value $q_0 = 150$ kPa.
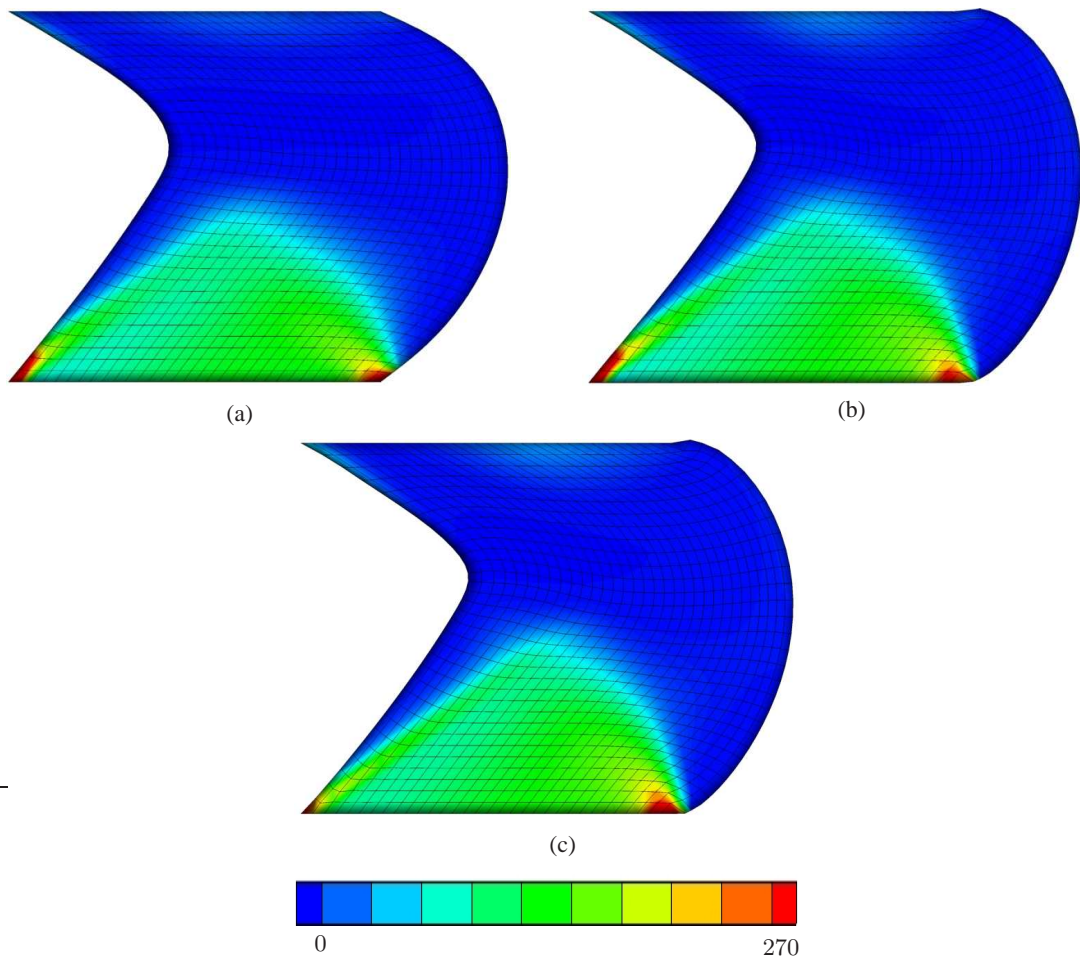
Figure 3.8: Fiber stress results for (a) $Q1$ (b) $Q1P0$ and (c) $Q1P0F0$ element formulations for pressure value $q_0 = 150$ kPa with mesh size 32 elements per edge.

34
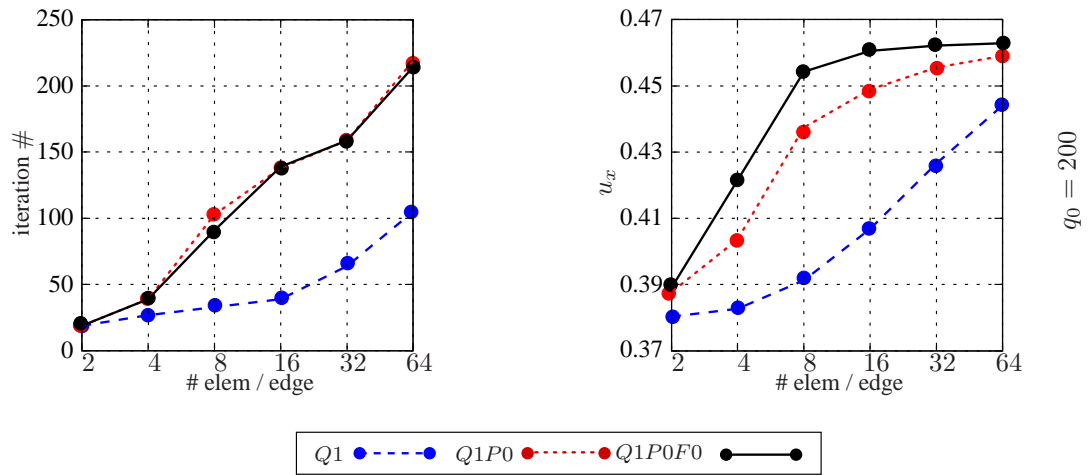
Figure 3.9: Comparison of the $Q1$, $Q1P0$ and $Q1P0F0$ element formulations for pressure value $q_0 = 200$ kPa.


(a)

(b)

(c)
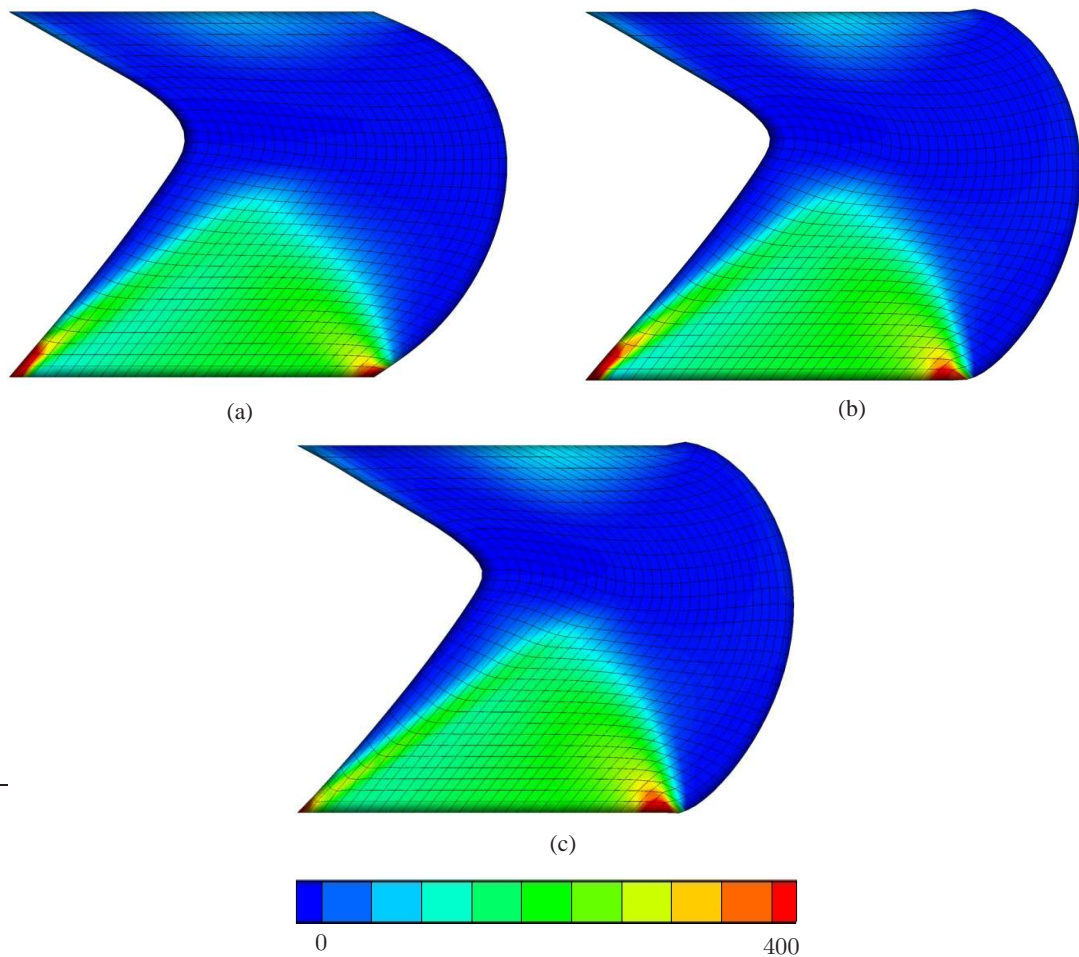
Figure 3.10: Fiber stress results for (a) $Q1$ (b) $Q1P0$ and (c) $Q1P0F0$ element formulations for pressure value $q_0 = 200$ kPa with mesh size 32 elements per edge.

Table 3.2: Comparison of CPU times for *Q1*, *Q1P0* and *Q1P0F0* formulations with different mesh sizes at $q_0 = 200$ kPa.

	2×2	4×4	8×8	16×16	32×32	64×64
Q1	0.03 s	0.16 s	0.90 s	6.44 s	27.49 s	165.57 s
Q1P0	0.04 s	0.19 s	1.41 s	7.26 s	35.03 s	229.38 s
Q1P0F0	0.04 s	0.38 s	2.09 s	14.45 s	70.22 s	403.37 s

Figure 3.9 shows the results of the analyses conducted at $q_0 = 200$ kPa. *Q1* formulation is not convergent with the increased mesh resolution. Mesh convergence of the mid-displacement for increasing mesh density for *Q1P0F0* formulation is much better than *Q1P0* formulation. For example, *Q1P0F0* formulation reaches convergence at 16 elements per edge while *Q1P0* formulation reaches convergence at 64 elements per edge.

Moreover, Table 3.2 shows the comparison of CPU times for *Q1*, *Q1P0* and *Q1P0F0* formulations with different mesh sizes at $q_0 = 200$ kPa. Analysis of *Q1P0F0* formulation at 16 elements per edge takes 14.45 s while analysis of *Q1P0* formulation at 64 elements per edge takes 229.38 s. Therefore, when the results of Figure 3.9 and Table 3.2 are combined, it can be said that *Q1P0F0* formulation reaches mesh convergence at 14.45 s while *Q1P0* formulation reaches mesh convergence at 229.38 s.

Also, Figure 3.10 shows the fiber stress results at $q_0 = 200$ kPa for a mesh size of 32 elements per edge. Fiber stress magnitudes are much higher for the *Q1* and *Q1P0* formulations than *Q1P0F0* formulation.

Moreover, Figure 3.11 demonstrates displacement results in x-direction at $q_0 = 200$ kPa for mesh sizes of 16 and 32 elements per edge. When the displacement distribution for the *Q1* formulation is analyzed, increasing number of elements affects the displacement results, especially for *Q1* and *Q1P0* formulations. Moreover, *Q1P0F0* has a better displacement distribution at less number of elements with respect to *Q1* and *Q1P0* formulation.

When all figures are analyzed, it can be seen that *Q1* formulation is not convergent. There should be more number of elements for the mesh convergence of the *Q1* formulation. *Q1P0* and *Q1P0F0* formulations have same convergence rate at low level
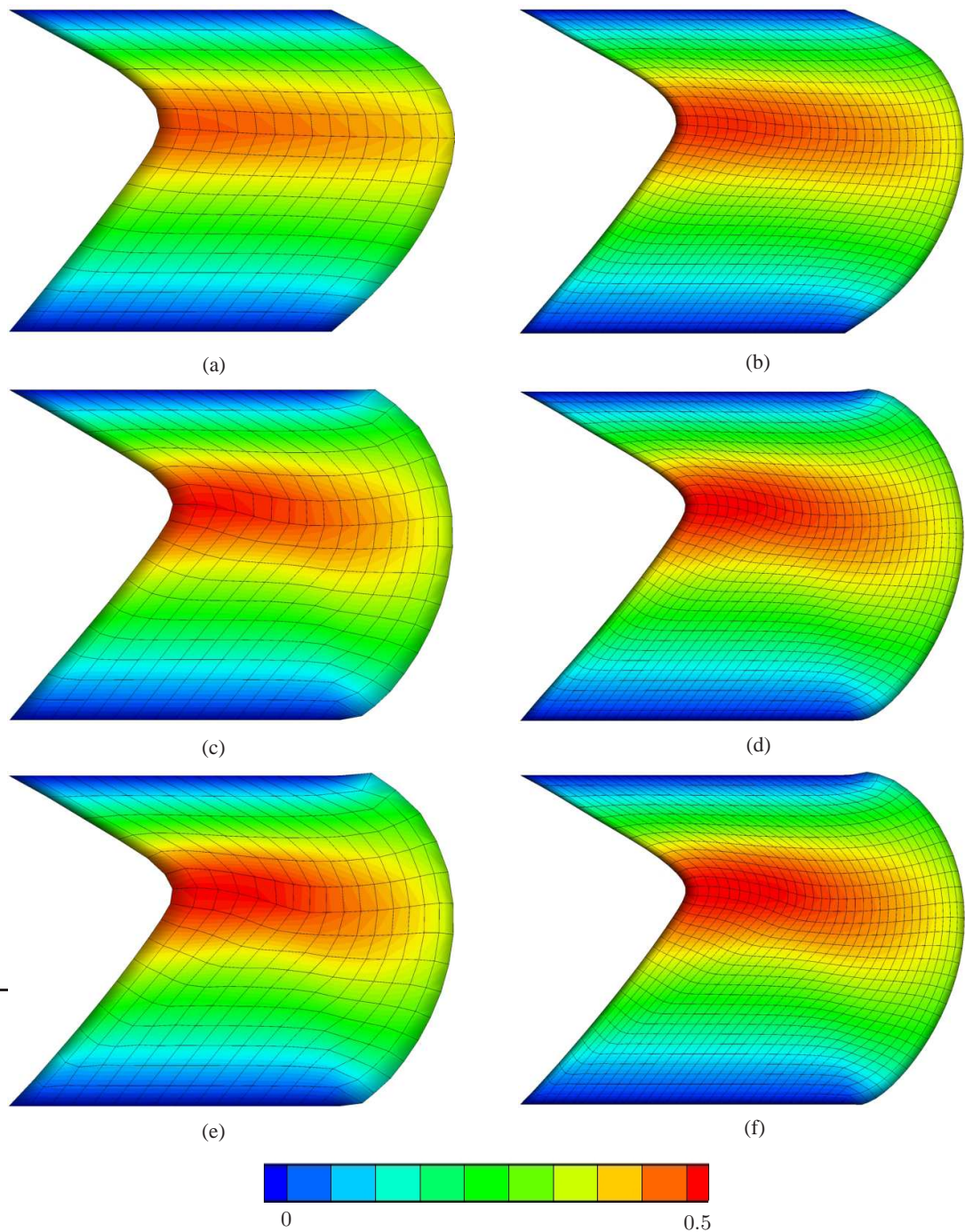
Figure 3.11: u_x results for (a) $Q1$ (c) $Q1P0$ and (e) $Q1P0F0$ element formulations with mesh size 16 elements per edge and (b) $Q1$ (d) $Q1P0$ and (f) $Q1P0FO$ element formulations with mesh size 32 elements per edge for pressure value $q_0 = 200$ kPa.

of pressure. However, *Q1P0F0* formulation converges to final displacement value at less number of elements when the load is increased. This fact decreases computation time by reducing number of the element needed for convergence.

Moreover, when the fiber stress results are analyzed from Figures 3.4, 3.6, 3.8 and 3.10, it is seen that fiber stress is lower for *Q1P0F0* formulation compared to other two formulations. This can be interpreted such that *Q1P0F0* formulation can extend much more compared to *Q1* and *Q1P0* formulations so fiber stress is much lower for proposed formulation because artificial stiffening effects occur for *Q1* and *Q1P0* formulations in inextensible region.

Therefore, the proposed formulation is the most robust among all alternatives, showing convergence with the less number of elements throughout the whole set of simulations, especially at the limits of incompressibility and inextensibility.

CHAPTER 4

IMPLEMENTATION OF THE MODEL

4.1 Model Description

In this chapter *Q1P0F0* formulation will be applied to an example of biological tissue which is arterial wall. Figure 4.1 shows the geometry and mesh of the arterial wall model.
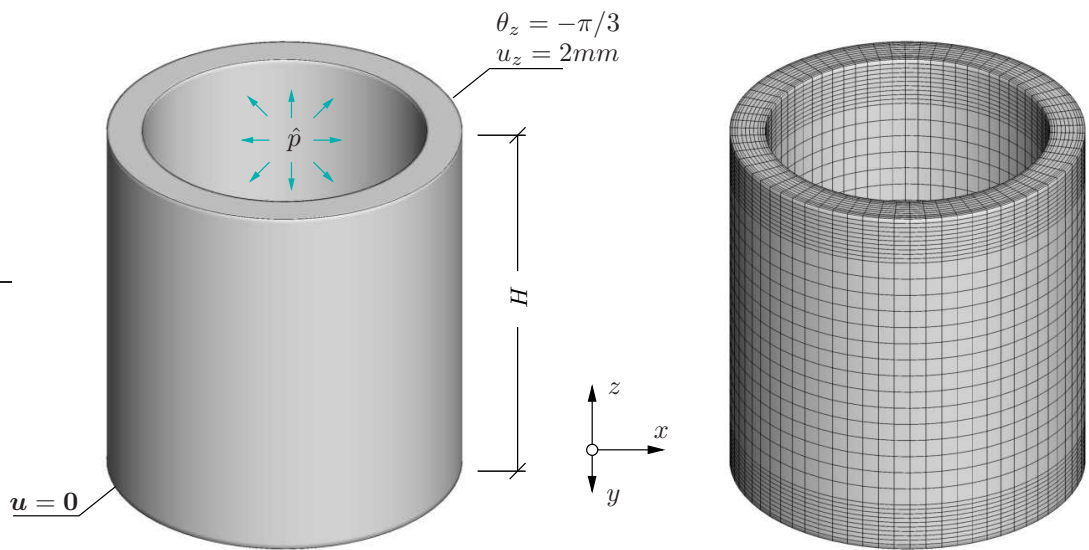
Figure 4.1: Geometry and mesh of the artery.

As it is mentioned in the introduction chapter, arterial wall consists of three main layers as intima, media and adventitia. Figure 4.2 shows the layers of the arterial wall in terms of mesh configuration. Green elements represent the intima layer, yellow elements represent the media layer, and blue elements represent the adventitia layer as shown in Figure 4.2. In radial direction, intima layer contains 3 elements in a total thickness of 0.3 mm, media layer contains 5 elements in a total thickness of 0.8

Table 4.1: Geometrical parameters.

Parameter	Value	Unit	Parameter	Value	Unit
d_o^A	14.0	[mm]	d_i^A	13.4	[mm]
d_o^M	13.4	[mm]	d_i^M	11.8	[mm]
d_o^I	11.8	[mm]	d_i^I	11.2	[mm]
H	15.0	[mm]			

mm and adventitia layer contains 3 elements in a total thickness of 0.3 mm. Totally, intima, media and adventitia layers have 7350, 12250 and 7350 elements, respectively. The total number of elements used in the analysis is 26950.
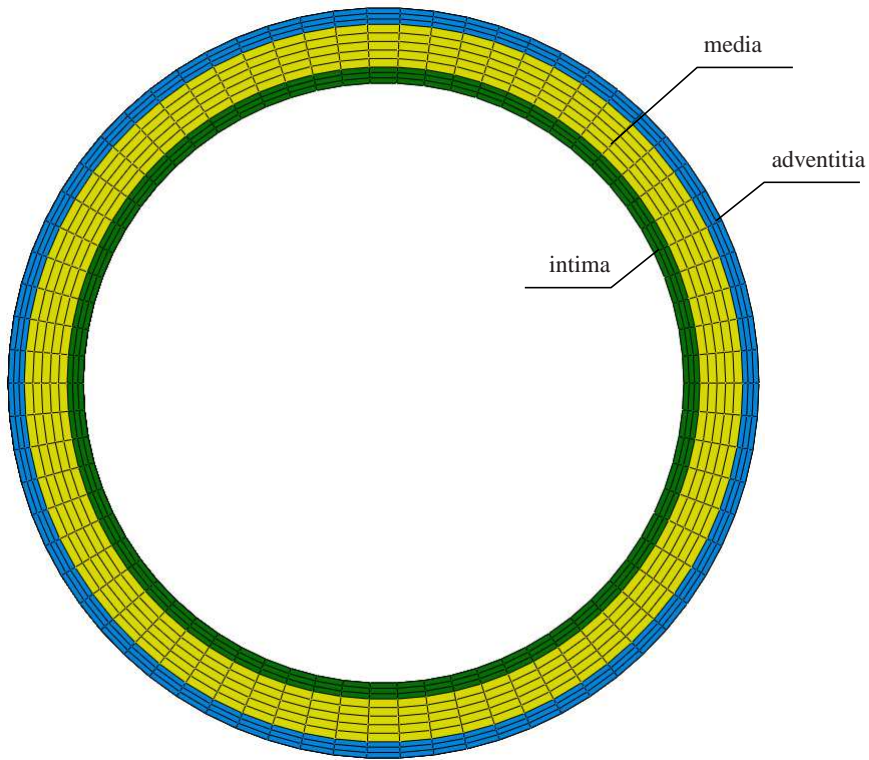
Figure 4.2: Layers of the artery as intima, media and adventitia.

Geometrical parameters of the artery are given in Table 4.1. d_o^A and d_i^A represent outer and inner diameters of the adventitia layer. d_o^M and d_i^M represent outer and inner diameters of the media layer. Also, d_o^I and d_i^I represent the outer and inner diameters of the intima layer. Moreover, H stands for the height of the cylinder. Geometrical parameters reflect an real artery geometry taken from [26].

Each layer of the artery behaves differently. Also, fibers are located in each layer with
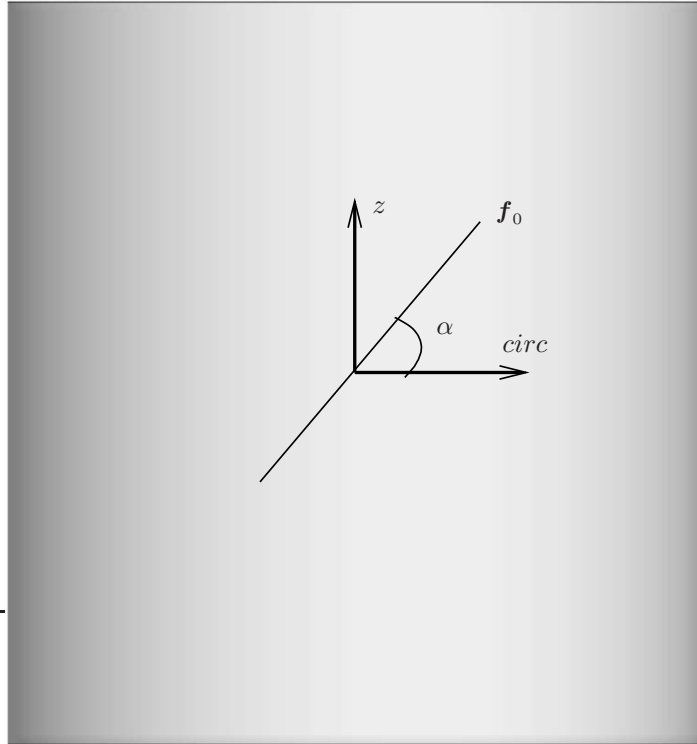
Figure 4.3: Fiber angle configuration.
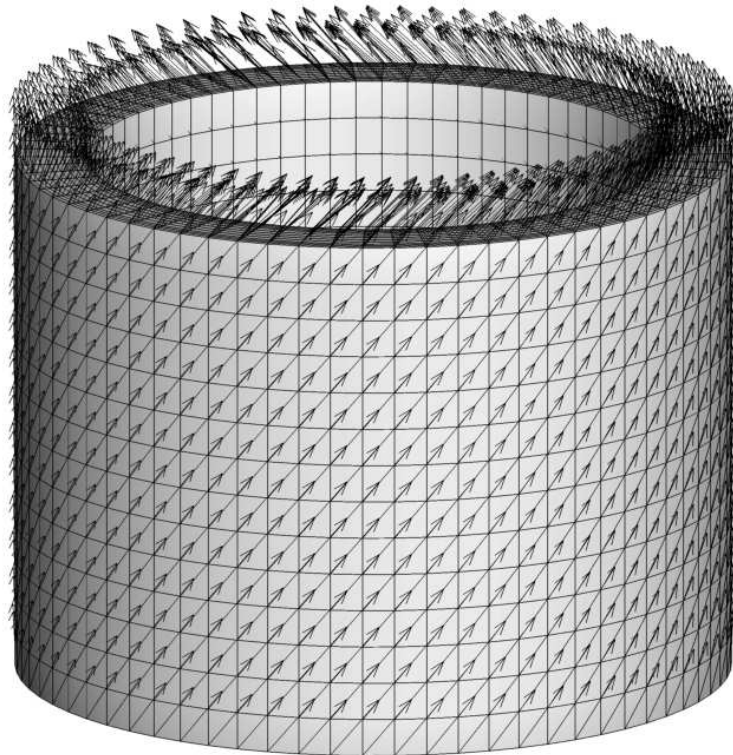
Figure 4.4: Fiber angle configuration in the mesh.

Table 4.2: Material parameters of intima layer.

| Parameter	Value	Unit	Parameter	Value	Unit
κ^I	10^4	[kPa]	$\mu^I = 2c_1^I$	33.86	[kPa]
k_1^I	7.79	[kPa]	k_2^I	139.1	[-]
α^I	46.8^o	[-]			

Table 4.3: Material parameters of media layer.

Parameter	Value	Unit	Parameter	Value	Unit
κ^M	10^4	[kPa]	$\mu^M = 2c_1^M$	16.08	[kPa]
k_1^M	11.68	[kPa]	k_2^M	7.18	[-]
α^M	41°	[-]			

different angles. Angle α is located in circumferential-axial plane of the cylinder and it is defined as angle between fiber direction and circumferential axis as it can be seen from Figure 4.3. Also, fiber angle configuration is given in the mesh of the artery in Figure 4.4.

Material parameters of each layer are given in Tables 4.2, 4.3 and 4.4. κ is bulk modulus, μ is shear modulus of each layer. Moreover, k_1 and k_2 are material constants for anisotropic free energy function. Also, fiber angle α is given for each layer. These parameters, which are taken from the work of Holzapfel [22], reflect behavior of the human aortas.

Behavior of the arterial wall under the effects of multiple loadings will be analyzed in this chapter. Loads to be applied are axial stretch, twist of the top surface and internal pressure. In normal conditions, axial stretch expected for arterial wall is almost 10 percent so 2 mm axial displacement (u_z) is applied from the top ($z = H$) surface as it can be seen from Figure 4.1. Also, -60° twist around z axis is given from the top ($z = H$) surface of the cylinder. Finally, internal pressure is given to reflect the

Table 4.4: Material parameters of adventitia layer.

Parameter	Value	Unit	Parameter	Value	Unit
κ^A	10^4	[kPa]	$\mu^A = 2c_1^A$	3.77	[kPa]
k_1^A	0.36	[kPa]	k_2^A	45.88	[-]
α^A	50.1^o	[-]			

Table 4.5: Applied loads and displacements.

Case	Parameter	Value	Unit	Parameter	Value	Unit	Parameter	Value	Unit
1	$\hat{p}$	7.5	[kPa]	u_z	2	[mm]	θ_z	$-\pi/3$	[rad]
2	$\hat{p}$	10	[kPa]	u_z	2	[mm]	θ_z	$-\pi/3$	[rad]
3	$\hat{p}$	15	[kPa]	u_z	2	[mm]	θ_z	$-\pi/3$	[rad]

blood pressure of the artery. As a boundary condition, all displacements of the bottom $(z = 0)$ surface of the cylinder are restrained.

Blood pressure of human arteries can be altered. For a healthy human artery, blood pressure changes between 7.5-15 kPa. Analyses will be conducted for different pressure values by keeping twist and axial stretch constant in order to analyze the effects of blood pressure deeply. Therefore 3 different load cases will be applied by only changing pressure and keeping other loads constant as it can be seen from Table 4.5.

4.2 Results

In the following subsections, results of three different cases will be presented, as summarized in Table 4.5. Also, comparison of the three different element formulations (*Q1*, *Q1P0*, *Q1P0F0*) studied in Chapter 3 will be conducted for load case 3 to show the behavior of the formulations in real artery configuration in the final subsection.

4.2.1 Case 1

In this section, results for a relatively low pressure $\hat{p} = 7.5$ kPa will be demonstrated with the other applied displacements. Radial displacement and tangential stress results are given in order to demonstrate behavior of the arterial wall.

Figure 4.5 represents the radial displacement results for step time increments $0.24t$, $0.48t$, $0.72t$ and $1.0t$. The load given in case 1 of Table 4.5 is reached by increasing from zero load to 100% load incrementally in a time of t. For instance, 24% of the load is applied at the instant of $0.24t$. When the results are analyzed for the time $1.0t$, the maximum radial displacement of the outer surface of the cylinder is about 3.15
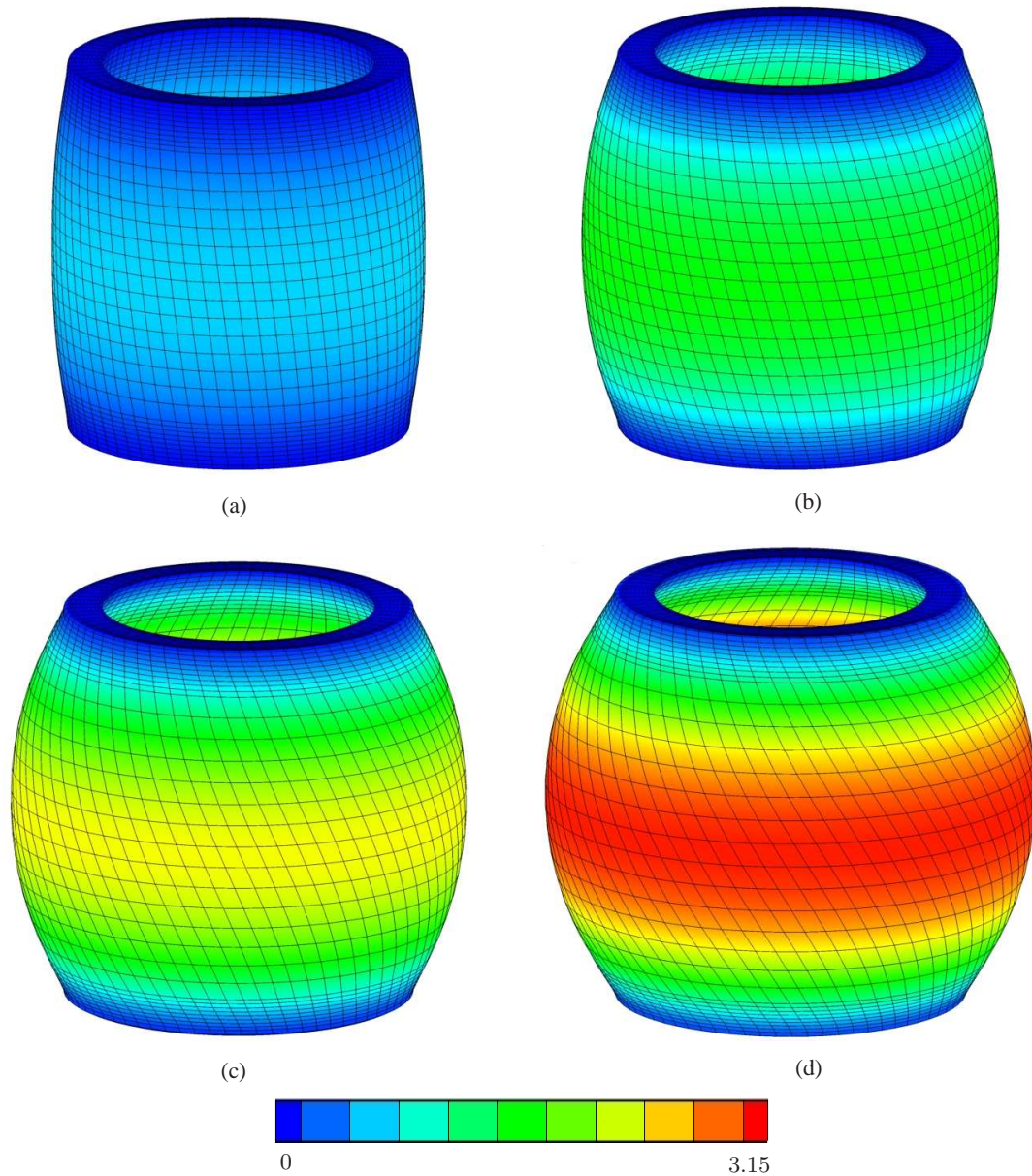
Figure 4.5: Radial displacement results (mm) for step time (a) $0.24t$ (b) $0.48t$ and (c) $0.72t$ (d) $1.0t$ for loadings $\hat{p} = 7.5$ kPa, $u_z = 2$ mm, $\theta_z = -\pi/3$.

mm.

Also, Figure 4.6 shows the tangential stress results for the loads given in case 1 of Table 4.5. For demonstration purposes, half of the cylinder is given to see the results of the inner layer more clearly. As it can be seen from Figure 4.6, the inner layer intima has higher tangential stress with respect to other layers. However, the difference between tangential stresses of the layers are comparable, respectively.

44
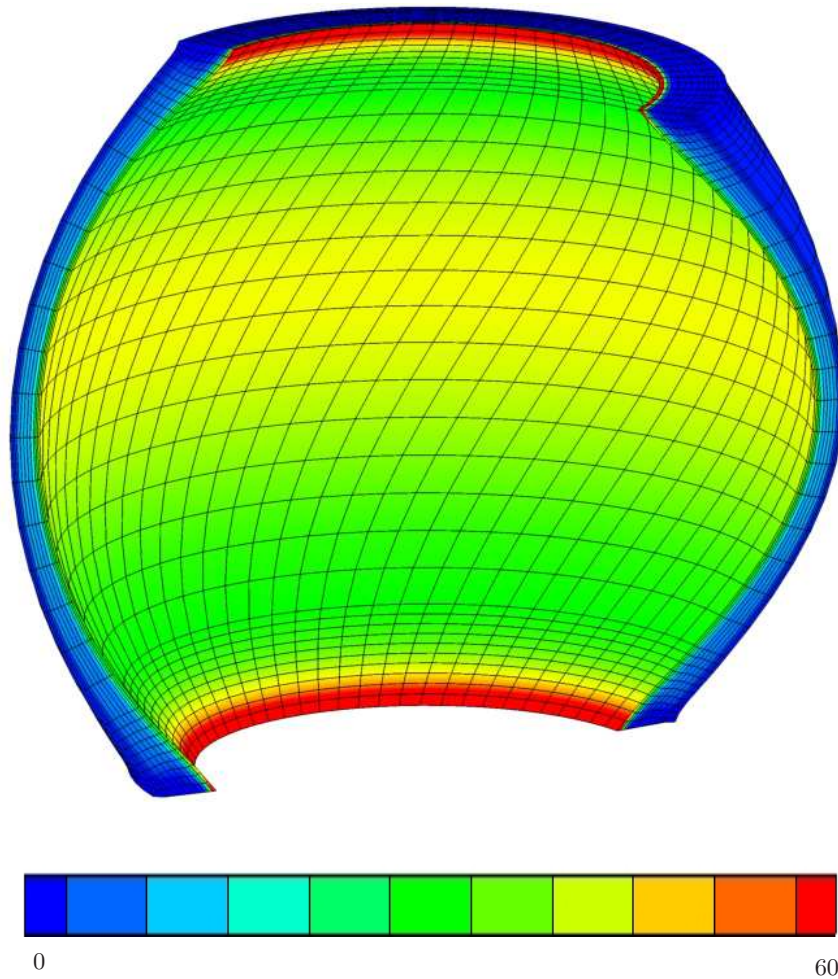
Figure 4.6: Tangential stress results (kPa) for $\hat{p} = 7.5$ kPa, $u_z = 2$ mm, $\theta_z = -\pi/3$.

4.2.2 Case 2

In this section, results for a relatively medium pressure $\hat{p} = 10$ kPa will be demonstrated with the other applied displacements. Radial displacement and tangential stress results are given in order to demonstrate the behavior of the arterial wall.

Figure 4.7 represents the radial displacement results for the step time increments $0.24t$, $0.48t$, $0.72t$ and $1.0t$. When the results are analyzed for the time $1.0t$, the maximum radial displacement of the outer surface of the cylinder is about 3.3 mm.

Also, Figure 4.8 shows the tangential stress results for the loads given in case 2 of Table 4.5. For demonstration purposes, half of the cylinder is given to see the results of the inner layer more clearly. As it can be seen from Figure 4.8, the inner layer intima has much higher tangential stress with respect to other layers.
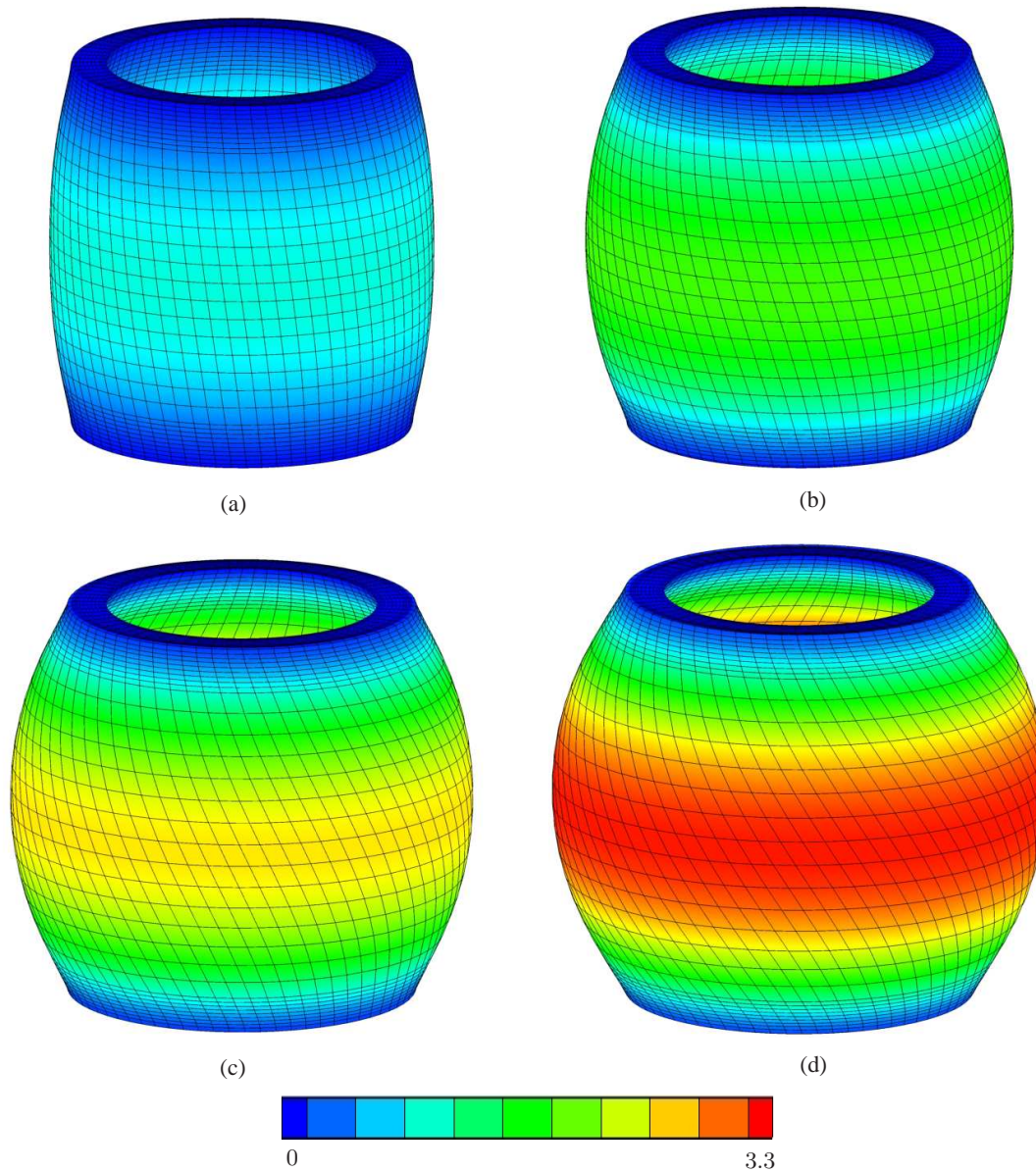
Figure 4.7: Radial displacement results (mm) for step time (a) $0.24t$ (b) $0.48t$ and (c) $0.72t$ (d) $1.0t$ for loadings $\hat{p} = 10$ kPa, $u_z = 2$ mm, $\theta_z = -\pi/3$.

4.2.3 Case 3

In this section, results for a relatively high pressure $\hat{p} = 15$ kPa will be demonstrated with the other applied displacements. Radial displacement and tangential stress results are given in order to demonstrate the behavior of the arterial wall.

Figure 4.9 represents the radial displacement results for the step time increments $0.24t$, $0.48t$, $0.72t$ and $1.0t$. When the results are analyzed for the time $1.0t$, maxi-
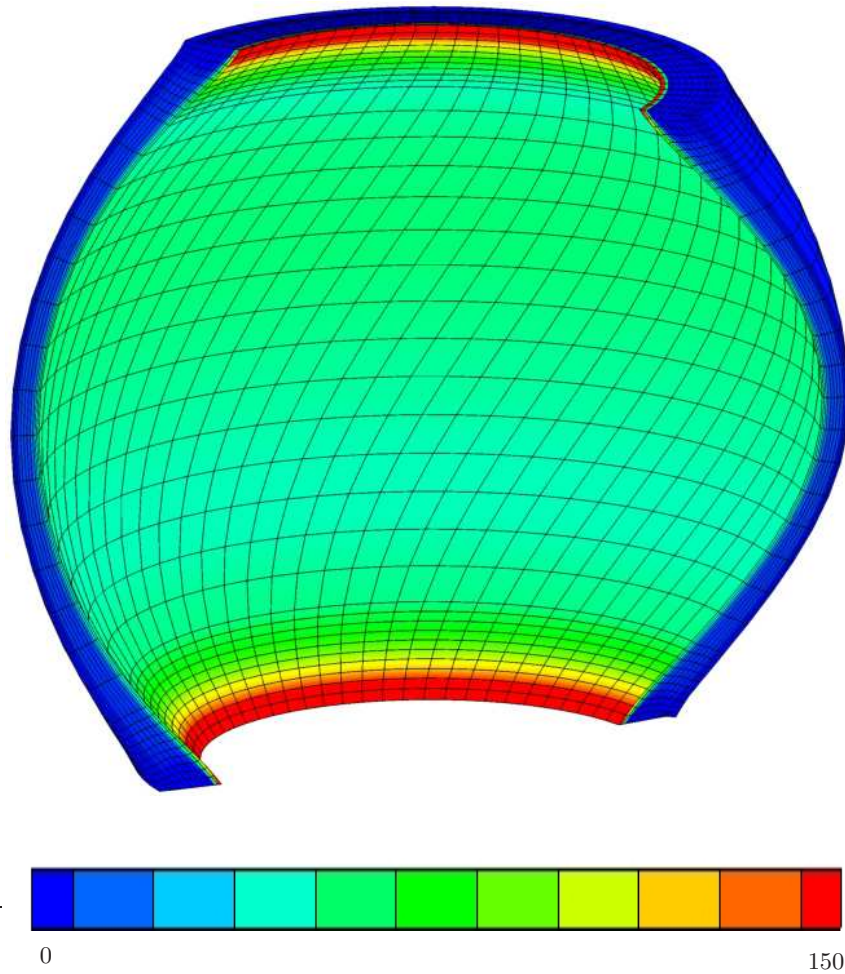
Figure 4.8: Tangential stress results (kPa) for $\hat{p} = 10$ kPa, $u_z = 2$ mm, $\theta_z = -\pi/3$.

mum radial displacement of the outer surface of the cylinder is about 3.5 mm.

Also, Figure 4.10 shows the tangential stress results for the loads given in case 3 of Table 4.5. For demonstration purposes, half of the cylinder is given to see the results of the inner layer more clearly. As it can be seen from the Figure 4.10, the inner layer intima has much higher tangential stress with respect to other layers.

When all three cases are compared, nonlinear behavior of the artery can be clearly observed from Figure 4.5, Figure 4.7 and Figure 4.9. The internal pressure is increased from 7.5 kPa up to 15 kPa while radial displacement is only increased from 3.15 mm to 3.5 mm at the outer surface of the cylinder. This fact shows inextensible behavior of arterial wall when the load is increased.

Also, when the tangential stress results are analyzed for three cases, stress of the
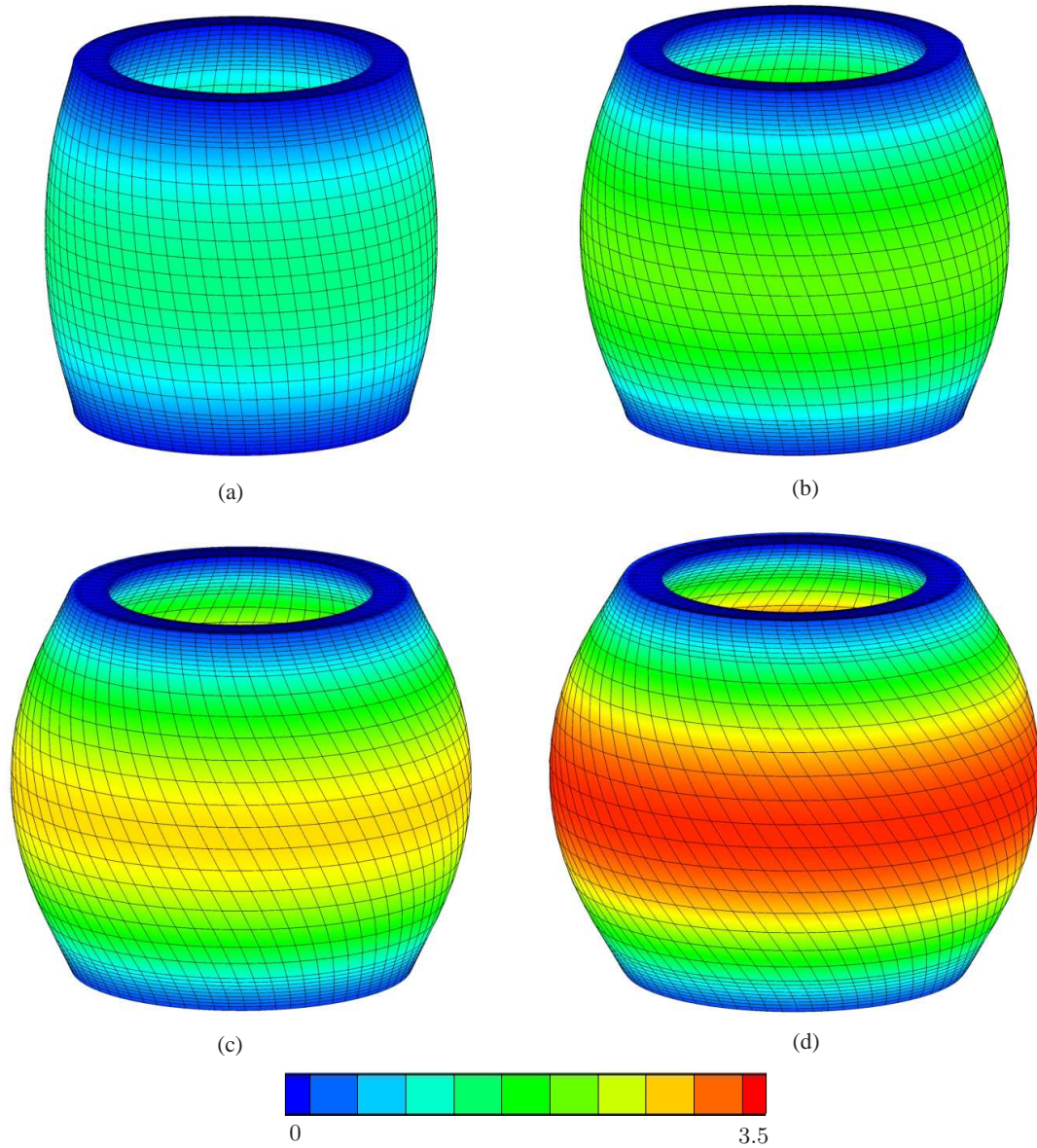
Figure 4.9: Radial displacement results (mm) for step time (a) $0.24t$ (b) $0.48t$ and (c) $0.72t$ (d) $1.0t$ for loadings $\hat{p} = 15$ kPa, $u_z = 2$ mm, $\theta_z = -\pi/3$.

inner layer, intima, has increased sharply with increasing pressure. Maximum tangential stress is increased from 60 kPa to 450 kPa by increasing internal pressure from 7.5 kPa to 15 kPa. However, middle layer media and outer layer adventitia are not significantly affected by the pressure increase.

All stress and displacement results indicate that the behavior of the arterial wall is in the limit of inextensibility with the increased load. Moreover, proposed formulation achieved to converge for all load cases successfully.
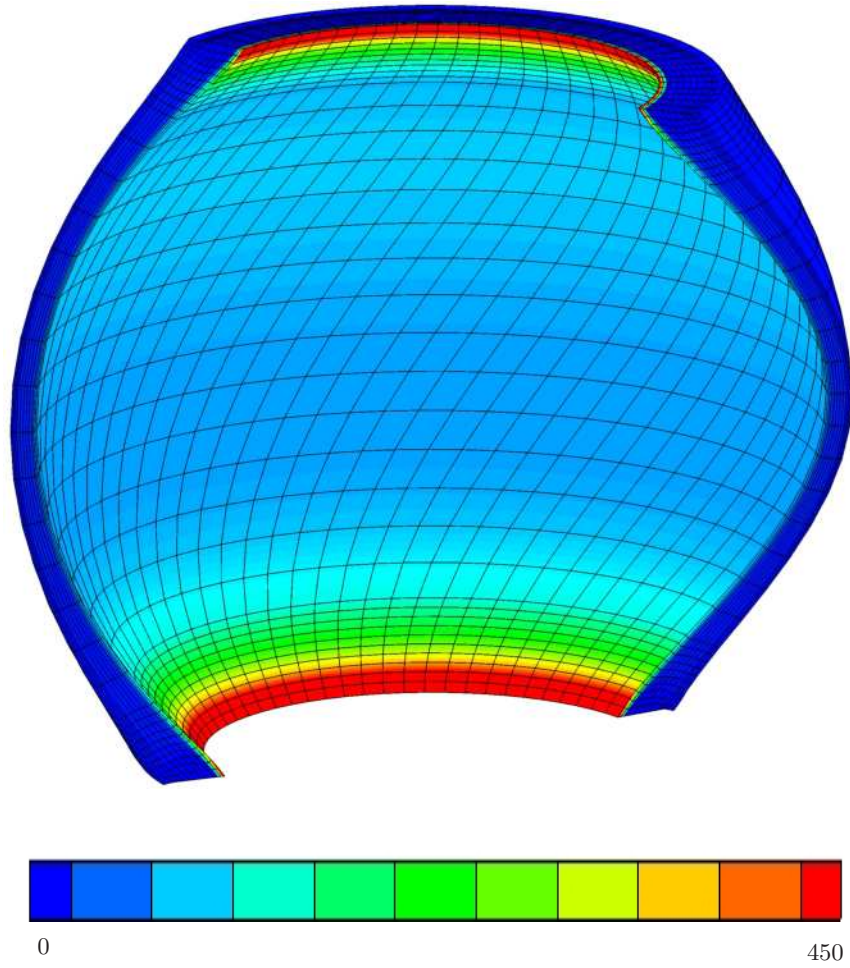
Figure 4.10: Tangential stress results (kPa) for $\hat{p} = 15$ kPa, $u_z = 2$ kPa, $\theta_z = -\pi/3$.

4.2.4 Comparison of the models for case 3

Comparison of the proposed formulation *Q1P0F0* with the *Q1*, *Q1P0* formulations, studied in Chapter 3, will also be conducted in this part of the chapter. The comparison will be studied to see the behavior of the three formulations for more realistic configuration of the artery. Load case 3 will be applied to the model for all formulations. Also, this comparison will be useful to see the behavior of the formulations for combined loading.

Figure 4.11 shows the radial displacement map for three formulations. Although minimum radial displacement is 0.00 mm, minimum limit of the legend is given as 3.00 mm to analyze the region which has radial displacements between 3.00 mm and 4.12 mm in detail and to compare results for inextensibility limit more clearly. When

49
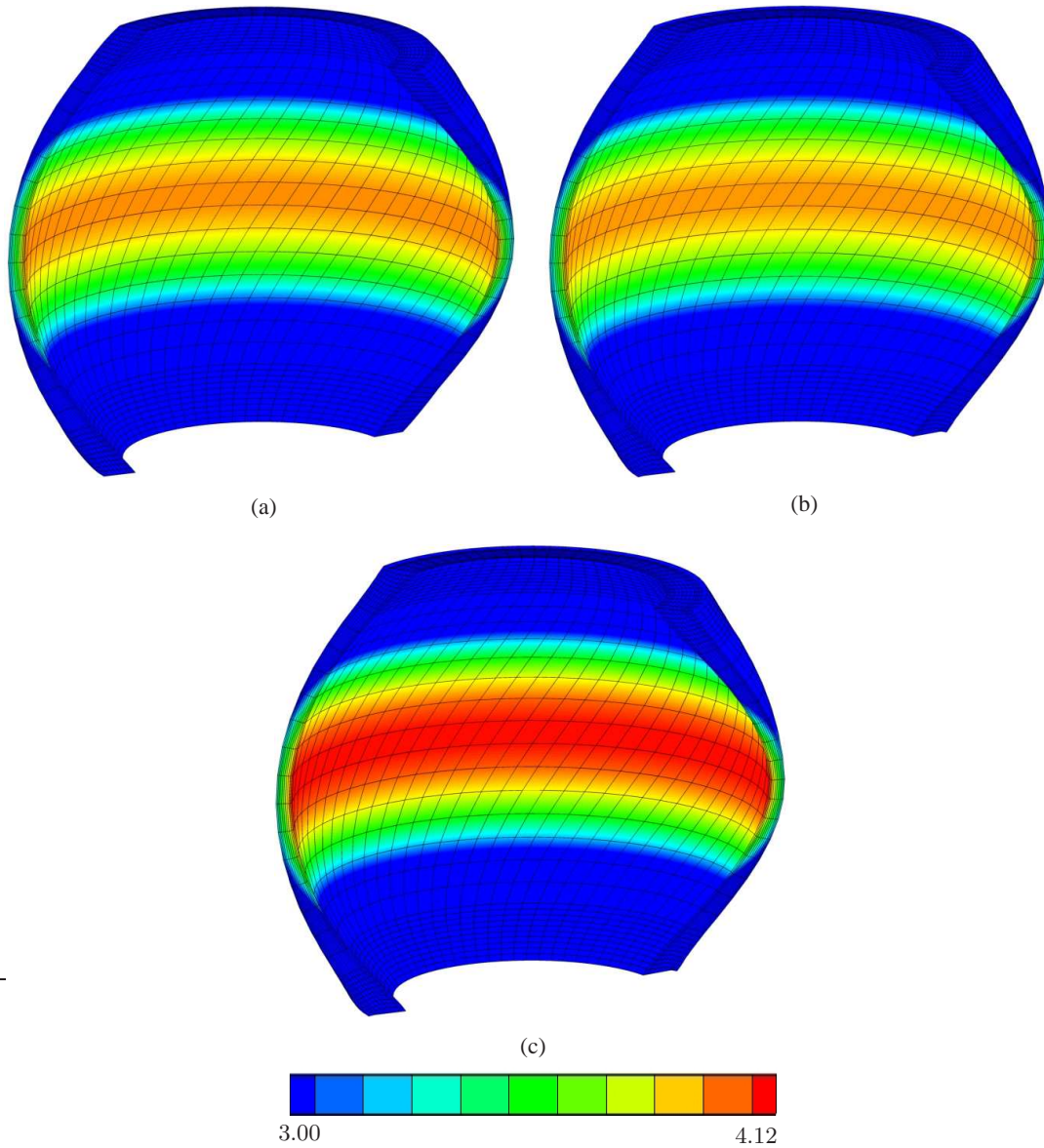
Figure 4.11: Radial displacement results (mm) for (a) $Q1$ (b) $Q1P0$ and (c) $Q1P0F0$ for loadings $\hat{p} = 15$ kPa, $u_z = 2$ kPa, $\theta_z = -\pi/3$.

the results of the *Q1*, *Q1P0*, *Q1P0F0* element formulations are compared from Figure 4.11, it is seen that proposed formulation, *Q1P0F0*, gives higher radial displacement results than *Q1*, *Q1P0* element formulations. *Q1*, *Q1P0* element formulations give maximum radial displacement about 3.96 mm while maximum radial displacement for *Q1P0F0* element formulation is 4.12 mm. To analyze more clearly the difference between results, it should be noted that 3.96 mm radial displacement is almost equal to the maximum radial displacement of inner surface of cylinder for *Q1P0F0* element formulation at load case 2 ($\hat{p} = 10$ kPa). Therefore, this means that the maximum

radial displacement of *Q1*, *Q1P0* element formulations at load case 3 ($\hat{p} = 15$ kPa) is equal to maximum radial displacement of *Q1P0F0* element formulation at load case 2 ($\hat{p} = 10$ kPa). This shows how proposed formulation can extend better in the inextensibility limit.

CHAPTER 5

CONCLUSION AND FUTURE WORK

5.1 Conclusion

In this study, a five field Hu-Washizu type variational principle for transversely aniso-
tropic materials in the quasi-incompressibility and quasi-inextensibility limit is pre-
sented. The main advantage of the proposed *Q1P0F0* formulation is the ease of ap-
plication at element level. The additional degrees of freedoms are condensed out with
numerical homogenization at element level. Also, matrix inversion is not needed for
the proposed formulation. Therefore, this fact enables quick and direct computation
of element stiffness matrix.

Moreover, *Q1P0F0* formulation does not need any extra kinematic assumptions so
application of the standard reinforcing model is very appropriate. Also, it is easy
to extend *Q1P0* formulation to *Q1P0F0* element formulation. A few additional al-
gebraic operations are needed to extend the formulation. Also, constitutive model,
which is appropriate to human arteries, was used to show performance of the formu-
lation for biological tissues.

In Chapter 3, the proposed, *Q1P0F0*, element formulation was compared with the
standard linear displacement element, (*Q1*), formulation and the mean dilatation ap-
proach denoted as *Q1P0* element formulation. Simple model was constructed for
comparison. A square block is loaded from one side with a pressure. Also, material
properties which is belong to human arterial walls are used. Formulations are com-
pared for different mesh sizes as 2, 4, 8, 16,32 and 64 elements per edge. Also, the
formulations are analyzed for 4 different loading magnitudes to show the behavior of

formulations in inextensibility limit. When the results are analyzed, it is clearly seen that proposed formulation is more robust and shows better performance for coarse meshes. Especially, the proposed formulation exhibit its advantages strongly at high level of the loads. High level of the loads means that the model is closed to the inextensibility limit.

After the validation of the proposed formulation, *Q1P0F0* element formulation was implemented to more realistic artery structure in Chapter 4. Performance of the formulation was tested for multiple loadings of the human arterial wall. These loadings include internal pressure, axial stretch and torsion. Three different values of the pressure were tested with the constant axial stretch and torsion. The aim of changing pressure was that internal pressure of the artery can be varied highly and its effects are trending topic in the research of the mechanics of artery. Therefore, three load cases were investigated and when the results of all load cases are analyzed, the proposed formulation achieved to converge for all three load cases successfully.

Moreover, as it is studied in the Chapter 3, one example is conducted for three element formulations as *Q1*, *Q1P0* and *Q1P0F0* for load case 3 of Chapter 4. The reason of this comparison is to show advantages of the proposed formulation in more realistic structure of biological tissues (human arterial wall). Realistic structure of a human arterial wall contains different layers with different material properties and fiber angles and different loading types. Load case 3 is chosen for the comparison because highest load levels are included in load case 3. Radial displacements results were given for comparison for each element formulation. When the results of this study are analyzed, proposed *Q1P0F0* formulation gives better results compared to other two element formulations in terms of radial displacements because the proposed formulation can extend better in inextensibility limit without being affected from artificial stiffening.

Therefore, when all case studies of this thesis are investigated, *Q1P0F0* element formulation exhibit very good performance in normal conditions as well as in incompressibility and inextensibility limits.

5.2   Future Work

Q1P0F0 element formulation can also be used to model the damage. Therefore, future work of this study can be devoted to damage modelling of the fiber reinforced materials and biological tissues by using *Q1P0F0* element formulation.

REFERENCES

[1] J. E. Adkins and R. S. Rivlin. Large elastic deformations of isotropic materials X. Reinforcement by inextensible cords. *Philosophical Transactions of the Royal Society of London A: Mathematical, Physical and Engineering Sciences*, A248:201–223, 1955.

[2] F. Auricchio, L. B. da Veiga, C. Lovadina, and A. Reali. A stability study of some mixed finite elements for large deformation elasticity problems. *Computer Methods in Applied Mechanics and Engineering*, 194:1075 – 1092, 2005.

[3] I. Babuška. The finite element method with lagrangian multipliers. *Numerische Mathematik*, 20:179–192, 1973.

[4] D. Balzani, S. Brinkhues, and G. A. Holzapfel. Constitutive framework for the modeling of damage in collagenous soft tissues with application to arterial walls. *Computer Methods in Applied Mechanics and Engineering*, 213:139 – 151, 2012.

[5] K. Bathe. The inf–sup condition and its evaluation for mixed finite element methods. *Computers and Structures*, 79:243–252, 2001.

[6] T. Belytschko and L. P. Bindeman. Assumed strain stabilization of the eight node hexahedral element. *Computer Methods in Applied Mechanics and Engineering*, 105:225 – 260, 1993.

[7] T. Belytschko, J. S.-J. Ong, W. K. Liu, and J. M. Kennedy. Hourglass control in linear and nonlinear problems. *Computer Methods in Applied Mechanics and Engineering*, 43:251 – 276, 1984.

[8] J. Betten. *Formulation of Anisotropic Constitutive Equations*, pages 228–250. Springer, Vienna, 1987. CISM Course no 292.

[9] J.-P. Boehler. A simple derivation of representations for non-polynomial constitutive equations in some cases of anisotropy. *ZAMM - Zeitschrift für Angewandte Mathematik und Mechanik*, 59:157–167, 1979.

[10] Boeing. Advanced composite use. www.boeing.com/commercial/787/by-design/. Accessed: 2018-02-28.

[11] F. Brezzi. On the existence, uniqueness and approximation of saddle-point problems arising from lagrangian multipliers. *Revue francaise d'automatique informatique recherche operationnelle Analyse numerique*, 8:129–151, 1974.

[12] H. Dal. Quasi-incompressible and quasi-inextensible element formulation for transversely isotropic materials. *International Journal for Numerical Methods in Engineering*, In review, 2018.

[13] H. Dal and M. Kaliske. Bergström–boyce model for nonlinear finite rubber viscoelasticity: theoretical aspects and algorithmic treatment for the fe method. *Computational Mechanics*, 44:809–823, 2009.

[14] W. Ehlers and G. Eipper. The simple tension problem at large volumetric strains computed from finite hyperelastic material laws. *Acta Mechanica*, 130:17–27, 1998.

[15] M. F. F. Brezzi. *Mixed and hybrid finite element methods*. Springer–Verlag, 1991.

[16] B. Fereidoonnezhad, R. Naghdabadi, and G. A. Holzapfel. Stress softening and permanent deformation in human aortas: Continuum and computational modeling with application to arterial clamping. *Journal of The Mechanical Behaviors of Biomedical Materials*, 61:600 – 616, 2016.

[17] R. Flory. Thermodynamic relations for highly elastic materials. *Transactions of the Faraday Society*, 57:829–838, 1961.

[18] T. C. Gasser, R. W. Ogden, and G. A. Holzapfel. Hyperelastic modelling of arterial layers with distributed collagen fibre orientations. *Journal of the Royal Society Interface*, 3:15 – 35, 2005.

[19] S. Glaser and F. Armero. On the formulation of enhanced strain finite elements in finite deformations. *Engineering Computations*, 14:759–791, 1997.

[20] O. Gültekin. Phase field approach to the fracture of anisotropic medium. Master's thesis, University of Stuttgart, 2013.

[21] J. Helfenstein, M. Jabareen, E. Mazza, and S. Govindjee. On non-physical response in models for fiber-reinforced hyperelastic materials. *International Journal of Solids and Structures*, 47:2056–2061, 2010.

[22] G. A. Holzapfel. *Microstructure and mechanics of human aortas in health and disease*, pages 157–192. Springer Nature, Switzerland, 2017.

[23] G. A. Holzapfel, T. C. Gasser, and R. W. Ogden. A new constitutive framework for arterial wall mechanics and a comparative study of material models. *Journal of Elasticity*, 61:1–48, 2000.

[24] G. A. Holzapfel, T. C. Gasser, and M. Stadler. A structural model for the viscoelastic behavior of arterial walls: Continuum formulation and finite element analysis. *European Journal of Meachanics A/Solids*, 21:441 – 463, 2002.

[25] G. A. Holzapfel and R. W. Ogden. Constitutive modelling of passive myocardium: a structurally based framework for material characterization. *Philosophical Transactions of The Royal Society A*, 367:3445 – 3475, 2009.

[26] G. A. Holzapfel and R. W. Ogden. Modelling the layer-specific three-dimensional residual stresses in arteries, with an application to the human aorta. *Journal of the Royal Society Interface*, 7:787 – 799, 2009.

[27] T. J. R. Hughes. Generalization of selective integration procedures to anisotropic and nonlinear media. *International Journal for Numerical Methods in Engineering*, 15:1413–1418, 1980.

[28] T. J. R. Hughes. *The Finite Element Method*. Prentice Hall, Englewood Cliffs, New Jersey, 1987.

[29] J. Korelc and P. Wriggers. Consistent gradient formulation for a stable enhanced strain method for large deformations. *Engineering Computations*, 13:103–123, 1996.

[30] O. Ladyzhenskaya. *The Mathematical Theory of Viscous Incompressible Flow*, volume 76. Gordon and Breach, New York, 1969.

[31] K. Li, R. W. Ogden, and G. A. Holzapfel. An exponential constitutive model excluding fibers under compression: application to extension–inflation of a residually stressed carotid artery. *Mathematics and Meachanics of Solids*, 2017.

[32] D. S. Malkus and T. J. Hughes. Mixed finite element methods – reduced and selective integration techniques: A unification of concepts. *Computer Methods in Applied Mechanics and Engineering*, 15:63 – 81, 1978.

[33] J. E. Marsden and T. J. R. Hughes. *Mathematical Foundations of Elasticity*. Prentice-Hall, Englewood Cliffs, New Jersey, 1983.

[34] J. Merodio and R. W. Ogden. Material instabilities in fiber-reinforced nonlinearly elastic solids under plane deformation. 54:525–552, 2002.

[35] J. Merodio and R. W. Ogden. Instabilities and loss of ellipticity in fiber-reinforced compressible nonlinearly elastic solids under plane deformation. 40:4707–4727, 2003.

[36] C. Miehe. Aspects of the formulation and finite element implementation of large strain isotropic elasticity. 37:1981–2004, 1994.

[37] C. Miehe, F. Aldakheel, and S. Mauthe. Mixed variational principles and robust finite element implementations of gradient plasticity at small strains. *International Journal for Numerical Methods in Engineering*, 94:1037–1074, 2013.

[38] C. Miehe, S. Teichtmeister, and F. Aldakheel. Phase-field modelling of ductile fracture: a variational gradient-extended plasticity-damage theory and its micromorphic regularization. *Philosophical Transactions of the Royal Society of London A: Mathematical, Physical and Engineering Sciences*, 374(2066), 2016.

[39] C. Miehe, F. Welschinger, and F. Aldakheel. Variational gradient plasticity at finite strains. part ii: Local–global updates and mixed finite elements for additive plasticity in the logarithmic strain space. *Computer Methods in Applied Mechanics and Engineering*, 268:704 – 734, 2014.

[40] J. C. Nagtegaal, D. M. Parks, and J. R. Rice. On numerically accurate finite element solutions in the fully plastic range. *Computer Methods in Applied Mechanics and Engineering*, 4:153–177, 1974.

[41] R. W. Ogden. Large deformation isotropic elasticity: on the correlation of theory and experiment for compressible rubberlike solids. *Proceedings of the Royal Society of London A: Mathematical, Physical and Engineering Sciences*, 328:567–583, 1972.

[42] T. H. H. Pian. Derivation of element stiffness matrices by assumed stress distributions. *AIAA Journal*, 2:1333–1336, 1964.

[43] T. H. H. Pian and D.-P. Chen. Alternative ways for formulation of hybrid stress elements. *International Journal for Numerical Methods in Engineering*, 18:1679–1684, 1982.

[44] T. H. H. Pian and K. Sumihara. Rational approach for assumed stress finite elements. *International Journal for Numerical Methods in Engineering*, 20:1685–1695, 1984.

[45] N. Qi, H. Gao, R. W. Ogden, N. A. Hill, G. A. Holzapfel, H. Han, and X. Luo. Investigation of the optimal collagen fibre orientation in human iliac arteries. *Journal of The Mechanical Behaviors of Biomedical Materials*, 52:108 – 119, 2015.

[46] G. Qiu and T. Pence. Remarks on the behavior of simple directionally reinforced incompressible nonlinearly elastic solids. *Journal of Elasticity*, 49:1–30, 1997.

[47] G. Y. Qiu and T. J. Pence. Loss of ellipticity in plane deformation of a simple directionally reinforced incompressible nonlinearly elastic solid. *Journal of Elasticity*, 49:31–63, 1997.

[48] S. Reese, M. Küssner, and B. D. Reddy. A new stabilization technique for finite elements in non-linear elasticity. *International Journal for Numerical Methods in Engineering*, 44:1617–1652, 1999.

[49] S. Reese and P. Wriggers. A stabilization technique to avoid hourglassing in finite elasticity. *International Journal for Numerical Methods in Engineering*, 48:79–109, 2000.

[50] J. Schröder and P. Neff. Invariant formulation of hyperelastic transverse isotropy based on polyconvex free energy functions. *International Journal of Solids and Structures*, 40:401 – 445, 2003.

[51] J. Schröder, N. Viebahn, D. Balzani, and P. Wriggers. A novel mixed finite element for finite anisotropic elasticity; the ska-element simplified kinematics for anisotropy. *Computer Methods in Applied Mechanics and Engineering*, 310:475 – 494, 2016.

[52] L. R. Scott and M. Vogelius. Norm estimates for a maximal right inverse of the divergence operator in spaces of piecewise polynomials. *Mathematical Modelling and Numerical Analysis*, 19:11–43, 1985.

[53] J. Simó, F. Armero, and R. Taylor. Improved versions of assumed enhanced strain tri-linear elements for 3d finite deformation problems. *Computer Methods in Applied Mechanics and Engineering*, 110:359 – 386, 1993.

[54] J. C. Simó and F. Armero. Geometrically non-linear enhanced strain mixed methods and the method of incompatible modes. *International Journal for Numerical Methods in Engineering*, 33:1413–1449, 1992.

[55] J. C. Simó and T. J. R. Hughes. On the variational foundations of assumed strain methods. *Journal of Applied Mechanics*, 53:51–54, 1986.

[56] J. C. Simó and M. S. Rifai. A class of mixed assumed strain methods and the method of incompatible modes. *International Journal for Numerical Methods in Engineering*, 29(8):1595–1638, 1990.

[57] J. C. Simó and R. L. Taylor. Quasi-incompressible finite elasticity in principal stretches. continuum basis and numerical algorithms. *Computer Methods in Applied Mechanics and Engineering*, 85:273–310, 1991.

[58] J. C. Simó, R. L. Taylor, and K. S. Pister. Variational and projection methods for the volume constraint in finite deformation elasto–plasticity. 51:177–208, 1985.

[59] H. Weisbecker, D. M. Pierce, P. Regitnig, and G. A. Holzapfel. Layer-specific damage experiments and modeling of human thoracic and abdominal aortas with non-atherosclerotic intimal thickening. *Journal of The Mechanical Behaviors of Biomedical Materials*, 12:93 – 106, 2012.

[60] J. A. Weiss, B. N. Maker, and S. Govindjee. Finite element implementation of incompressible, transversely isotropic hyperelasticity. *Computer Methods in Applied Mechanics and Engineering*, 135:107 – 128, 1996.

[61] P. Wriggers. *Nonlinear Finite Element Methods*. Springer–Verlag, 2008.

[62] P. Wriggers and S. Reese. A note on enhanced strain methods for large deformations. *Computer Methods in Applied Mechanics and Engineering*, 135:201 – 209, 1996.

[63] P. Wriggers, J. Schröder, and F. Auricchio. Finite element formulations for large strain anisotropic material with inextensible fibers. *Advanced Modeling and Simulation in Engineering Sciences*, 3:1–18, 2016.

[64] A. Zdunek, W. Rachowicz, and T. Eriksson. A novel computational formulation for nearly incompressible and nearly inextensible finite hyperelasticity. *Computer Methods in Applied Mechanics and Engineering*, 281:220–249, 2014.

[65] A. Zdunek, W. Rachowicz, and T. Eriksson. A five-field finite element formulation for nearly inextensible and nearly incompressible finite hyperelasticity. *Computers & Mathematics with Applications*, 72:25 – 47, 2016.

[66] O. C. Zienkiewicz, R. L. Taylor, and J. M. Too. Reduced integration technique in general analysis of plates and shells. *International Journal for Numerical Methods in Engineering*, 3:275–290, 1971.